UNIVERSITY OF OKLAHOMA

GRADUATE COLLEGE

INFLUENCE OF UNSTEADY BOUNDARY LAYER GROWTH BEHIND A NORMAL SHOCK WAVE ON THE DYNAMICS OF SPHERICAL WATER DROPLETS ON A SHOCK TUBE WALL

A THESIS

SUBMITTED TO THE GRADUATE FACULTY

in partial fulfillment of the requirements for the

Degree of

MASTER OF SCIENCE

By

MICHAEL CURRIE

Norman, Oklahoma

2024

INFLUENCE OF UNSTEADY BOUNDARY LAYER GROWTH BEHIND A NORMAL SHOCK WAVE ON THE DYNAMICS OF SPHERICAL WATER DROPLETS ON A SHOCK TUBE WALL

A THESIS APPROVED FOR THE

SCHOOL OF AEROSPACE AND MECHANICAL ENGINEERING

BY THE COMMITTEE CONSISTING OF

Dr. Hiroshi Ozawa, Chair

Dr. Ramkumar Parthasarathy

Dr. Prakash Vedula

Acknowledgements

I would first like to give my appreciation to Dr. Ozawa, who allowed me to operate his facilities, helped refine my experimental techniques for various experiments, and helped me understand the value of aerospace research. I would also like to give a huge thank you to the current members of the High Speed Aerothermodynamics Lab: Nick, Kosuke, and Ryo. You all were very helpful in aiding in my experiments while keeping the stress levels down. A big thanks also goes out to former lab members: Adam and Jacob, as their input during their time at the lab was also very useful.

An additional thank you goes out to Dr. Merchan-Merchan. With his kindness, he allowed me to borrow his Photron Fastcam Mini AX-100 for my experiments and provided input for different hydrophobic surfaces. I am indebted to him, as these are two of the most important facilities needed to properly conduct the experiments. I would also like to thank Dr. Parthasarathy and Dr. Vedula for taking the time to listen to my defense and provide any insight to make necessary improvements.

Finally, I am so thankful for my family and friends who supported me along the way. Anytime I was stressed, they were there to help me keep a level head. Finally, I am truly so thankful for my wonderful wife, Laura, as you motivated me to finish this thesis despite any of my frustrations. I am thankful for how patient you were with me no matter how long I stayed at the Lab to conduct my research. I love you so much.

Table of Contents

List of Figures

List of Tables

Abstract

The discrete increase of local pressure and temperature caused by a shock wave passing over a certain location in a shock tube allows for many potential investigations of the process of combustion. One of these investigations is the aero breakup of a liquid droplet, which could be a fuel droplet, and the instantaneous temperature rise results in potential combustion of the broken up fuel droplet. A specific study in how a wall-laden droplet breaks up in different freestream unit Reynolds number, diameter, and droplet attachment angle was conducted in order to characterize the different potential breakup modes seen by the aerobreakup of a droplet. Pointwise pressure data was employed to obtain freestream conditions, and shadowgraphs capturing the temporal evolution of the aerobreakup of a droplet on a shock tube wall in region 2 of a shock tube was observed. Edge detection was employed to quantify the droplet's deformation over time. It was observed that lower freestream Reynolds number and larger droplet diameters delayed the breakup of the droplet, despite being at comparable Weber numbers. The attachment angle also impacted the rate of deformation. Instabilities on the upstream side of the droplet were observed to generally decrease with an increase of diameter. These trends were observed for all possible conditions.

Chapter 1: Introduction

1.1: Shock waves

Shock waves occur when a disturbance travels through a gaseous medium, such as air, at a speed greater than the speed of sound in that medium. Typically, the gas dynamics of a disturbance moving at subsonic speeds result in pressure waves that spread outward at the speed of sound. However, when the disturbance exceeds the speed of sound, the pressure waves become compressed into a singular wave known as a shock wave or compression wave. Shock waves are characterized by a rapid increase in thermodynamic properties, such as temperature and pressure. In contrast, subsonic conditions exhibit more continuous changes in thermodynamic properties, represented by smooth curves. The discrete behavior caused by shock waves makes them quite notable for a myriad of research topics.

Due to the instantaneous change of pressure and temperature, a shock wave passing over a liquid droplet in a controlled environment is of high importance as the applications for fuel injection and combustion are very notable. Specifically, a liquid fuel droplet such as kerosene could be atomized by the high-pressure flow behind the shock wave, and the small particles produced by the breakup are ignited by the significant temperature gradient produced by the shock wave. As a result, the study of shock waves interacting with liquid droplets has been studied for the past 50 years. Typically, the focus of most of these studies is about the aero breakup of a spherical droplet in a freestream flow, as the resulting breakup is ideally atomized to small liquid particles known as aerosols. However, several problems arise when applying this idea to industry, as producing a timing mechanism to inject spherical droplets into a flow just before shockwave arrival can be difficult, and the sensitivity to initial conditions (on the order of a few hundred microseconds), makes it difficult to implement in real scenarios. Therefore, solutions to this problem are being investigated.

1.2: Shock Tubes

As discussed previously, shock waves are very important to understand for anything that may travel in the supersonic regime. Therefore, it is important to come up with an experimental facility that can produce a shock wave and record it through pressure and temperature measurements, along with flow visualization. A common device used that meets this criterion is a shock tube. A typical shock tube has a highly pressurized tank that contains a driver gas, or test gas. This gas is released from either a burstable diaphragm or fast acting valve, which is then released into a low-pressure section which is typically vacuumed well below atmospheric pressure.

When the high pressure tank is released by either the actuation of a pneumatic fast acting valve or eruption of a diaphragm, there is a compression wave caused by the significant pressure gradient that propagates downstream. Meanwhile, there is a series of expansion waves that travel upstream of the diaphragm section. The air downstream of the incident normal shockwave has the same conditions as the driven section had before the diaphragm was ruptured. Once the incident shockwave passes a certain location, flow is instantaneously accelerated to freestream conditions, where an increase in pressure and temperature is also observed. Once the incident shockwave hits the end wall of the shock tube, the shock wave is reflected. If the reflected normal shock wave passes over a certain location, any flow velocity that existed in the freestream is ideally brought to nearly zero velocity, while the local freestream pressure and temperature discretely increase again.

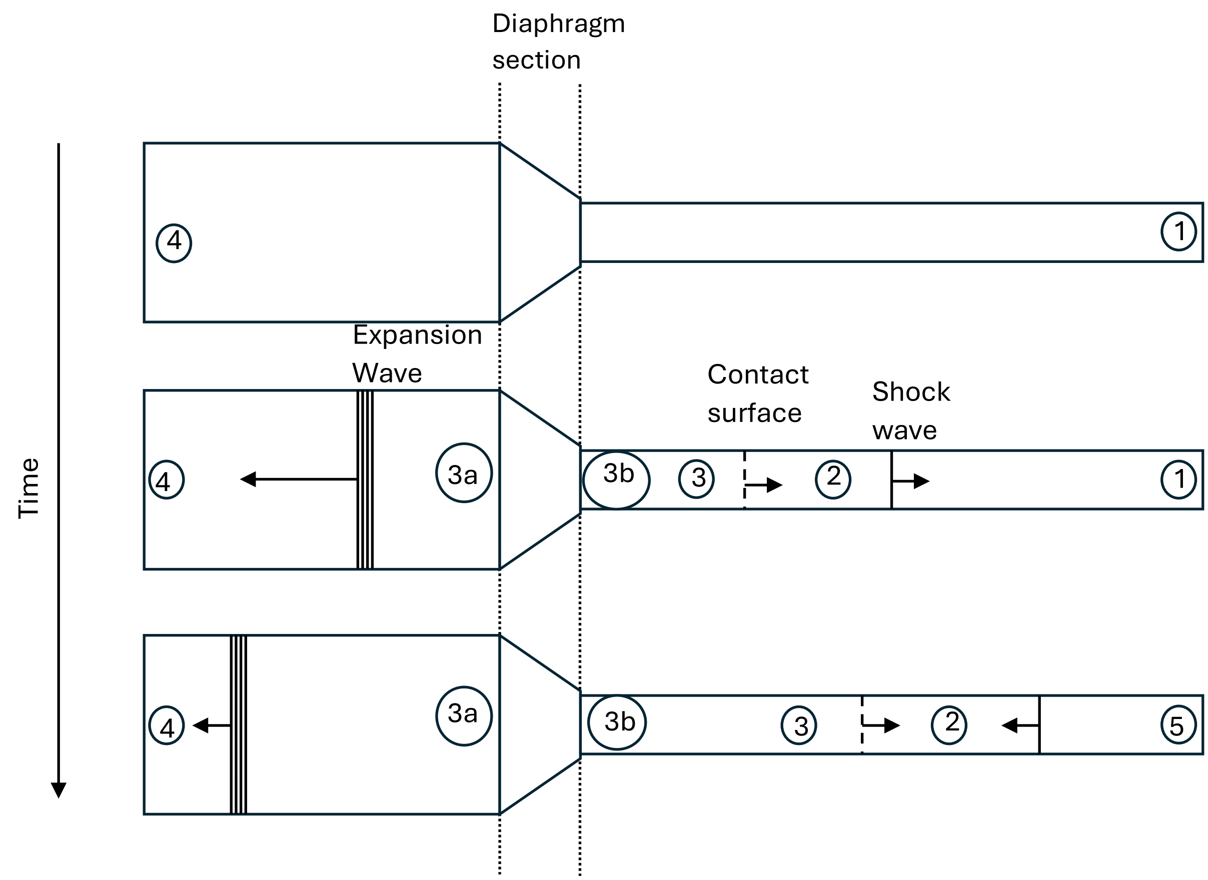

Figure 1: Diagram of Different Regions of the Shock Tube

Figure 1 illustrates the different regions considered in a shock tube. Before the diaphragm is ruptured, the driven section is a low pressure region referred to as region 1, while the driver section is a high pressure region referred to as region 4. After the diaphragm ruptures, the normal shockwave begins to travel towards the end wall. The regions downstream of the shockwave is still region 1, but just upstream of the shockwave is region 2, which denotes the freestream conditions behind the shockwave. After the shockwave hits the end wall and the reflected shock wave passes a specific location, the flow is officially in region 5. On the other hand, the driver gas that passes the expansion fan is considered to be in region 3. There is also the existence of a contact surface, which propagates downstream behind the shockwave, and is a discrete change in gas temperature and density, while the flow pressure and velocity remain constant across the contact surface. After the contact surface passes a specific location, it is considered to be in region 3. Eventually, the contact surface travelling downstream will collide with the reflected shockwave. This results in a pressure wave that moves downstream towards the end wall. This pressure wave will also be reflected, and collide with the contact surface, producing another pressure wave moving downstream. This will keep occurring until the collision is so weak that no pressure wave is produced. After the passing of the first pressure wave, the experimental test can be considered over. The expansion fan travelling towards the driver section must also be considered. After the fast removal of the diaphragm, the region in the driver tank in which the thermodynamic properties have yet to be altered by the expansion waves' arrival is considered region 4. All of these regions are to be considered for a shock tube experiment, as they all significantly vary the gas properties inside the tube. Therefore, it is important to document the gas properties for every test condition such that each region can be identified for a specific location.

Knowing the conditions in each region is very important in order to consider what test condition is needed for each experiment. The Rankine-Hugoniot equations are used to relate how pressure, temperature, velocity, and density change between each region. However, these equations have several assumptions, such as one-dimensional flow in a circular duct. Additionally, instability waves in the boundary layer cause further discrepancy between the theoretical values and the experimental results. Therefore, it is imperative to only consider the Rankine-Hugoniot relations as a preliminary study before finding the experimental test conditions in a shock tube.

1.3: Boundary Layer

When a fluid flows past a body or wall, there is a region near that body or wall where the freestream velocity gradient normal to the boundary is significantly large. This is a result from the no-slip condition, where the layer of fluid immediately next to the rigid body has zero relative velocity to the rigid body. The no-slip condition occurs when the viscosity of the fluid is non-negligible, such that the fluid produces some shear stress near the wall.

In a shock tube, this “boundary layer” forms by the walls. Since the flow is initiated by the passing of a shockwave, there is no boundary layer on the wall at a certain location until after the shock wave passes through that position. A visualization of a boundary layer developing in a shock tube can be visualized in the figure below:

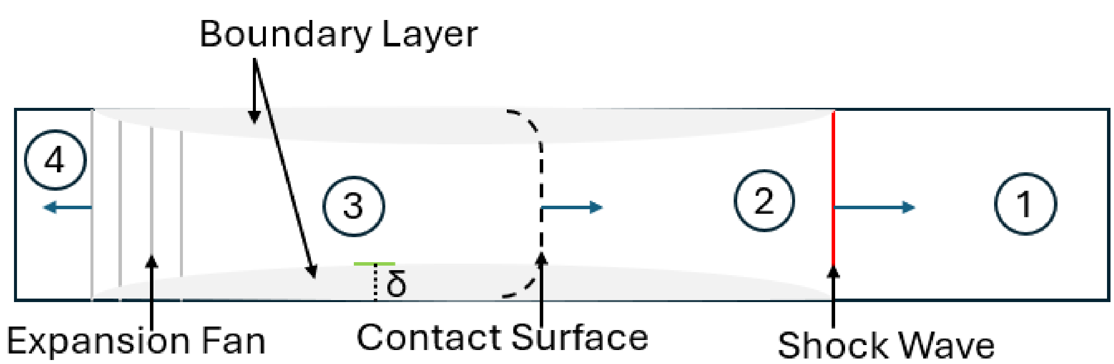

Figure 2: Illustration of the Boundary Layer Formation in a Shock Tube

After the incident shock wave passes a certain location, the boundary layer is laminar and grows at a consistent trend, which is typically predicted by [1], and is reflected in Figure 2. The boundary layer thickness δ is determined by the Reynolds number of the flow, along with the length behind the incident shockwave. Inside the boundary layer, the velocity distribution normal to the surface is significantly changing, and the rate of change is related to the viscosity of the fluid and shear stress. However, to account for compressibility, the boundary layer caused by airflow moving faster than M = 0.3 can be predicted by [2]. The laminarity of the boundary layer can be characterized by the boundary layer Reynolds number. Reynolds number is the ratio between inertial and viscous forces of the fluid and will be discussed later. The Reynolds number of a boundary layer depends on the length of the boundary layer. Additionally, for all flows there exists a critical Reynolds number which is the condition where flow transitions from laminar to turbulent. As a result, the boundary layer length has a significant impact on the laminarity of the boundary layer. For example, once the shockwave passes a specific location in the shock tube, the relations given by Mirels are accurate, since the length scale of the boundary layer is small, and as a result the Reynolds number of the boundary layer is likely less than the critical Reynolds number for transition. However, after a certain amount of time after the shockwave passes, the length scale becomes large enough to surpass the critical Reynolds number, and the boundary layer transitions from Laminar to Turbulent.

There are many resources that attempt to predict a turbulent boundary layer thickness such as [3-5]. Many of these resources also account for the compressibility of high-speed flow. However, since there is some variance between the predictions, and the turbulent boundary layer thickness being extremely sensitive to initial conditions, it is simply best to estimate it experimentally through flow visualization for example.

The boundary layer thickness growth for a specific location in a shock tube can be advantageous. Specifically, the variable thickness for controlled flows can result in an investigation of flow behaviors that have been uninvestigated previously. This is important because advantageous conditions could be produced by having the boundary layer grow over time.

1.4: Droplets

When a liquid is placed on a rigid surface, the cohesion between the molecules of the liquid cause surface tension. As a result, the liquid goes towards minimum potential energy, which yields a quasi-spherical geometry above the solid surface. Thus, there is an angle between the surface and the attachment angle between the droplet and the surface. The surface tension within the droplet depends on the cohesion force, and therefore strongly depends on the substance of the liquid. Additionally, Eovtos Law illustrates the surface tension's dependence on temperature as well. It is shown that it has a small effect but should still be considered for experiments.

The droplet's contact angle with the solid surface is also an important parameter to investigate. A droplet with a small contact angle (geometry similar to the surface), will have different behaviors than a droplet with a large contact angle (geometry similar to a sphere). In a shock tube, freestream flow behind the shock wave will be primarily unidirectional, or flow in one direction. Thus, if the droplet is perpendicular to the flow, a small contact angle will have a smaller reference area than a droplet with a larger contact angle. As a result, the fluid properties change. Additionally, when considering a boundary layer, a small contact angle will only experience shear forces that are tangential or downwards towards the wall. However, a contact angle greater than 90° will also experience shear forces in the upward direction, as the boundary layer can develop below the equator of the droplet. Therefore, the contact angle between the droplet and the wall is important to investigate.

1.5: Motivation

When a shock wave in a shock tube passes over a droplet, with the boundary layer developing behind the shock wave, there is a complex interaction between the shock wave, post wave freestream flow, boundary layer, and wall-laden droplet in the test section. The potential breakup or transformation of the wall-laden droplet is very important for several factors.

The most important motivation for this research is the combustion application. The aero breakup of a liquid droplet inside a shock tube has been studied extensively [6-13]. This is because with high speed turbomachinery such as ramjets and scramjets [14], and the high efficiency of atomized fuel [15], finding an advantageous method that can take high speed flow phenomena such as a normal shock wave inside a scramjet inlet to atomize and ignite the fuel will be highly beneficial. Fuel injections in high speed flow is also shown in [16], such as the figure below:

Figure 3: Application of Fuel Injection in a High Speed Flow

Most of the research for this specific application has been done with a spherical droplet, which has been conducted in several ways such as levitating a liquid droplet, timing the drop of a liquid droplet, and suspending a droplet from an injector. However, all of these come with the need for further investigation. Specifically, levitating a droplet inside the inlet of an engine for example is highly unrealistic, and timing the droplet to get hit by the incident shock wave in free fall requires precise measurements and ideal conditions to execute repeatably. Additionally, droplets sticking to the wall of a combustion chamber are likely to happen, so investigated how the droplets on a wall break up is important to understand.

1.6: Nondimensional Numbers

There exist a great number of nondimensional numbers that dictate the flow behavior inside a shock tube during an experiment. Two of the most important nondimensional numbers to consider in a shock tube flow are mach number and Reynolds number. The mach number is the ratio of a flow's velocity to the speed of sound. The speed of sound is determined by the gas composition and the absolute temperature of the gas. The velocity is the variable that is primarily controlled when investigating the effects of Mach Number in a flow. The velocity of a flow can be controlled in several ways, typically by controlling the cross sectional area in which the flow is contained in, along with the streamwise pressure gradient seen by the flow. Overall, the mach number of a flow has the following form:

$$M = \frac{V}{a} \tag{1}$$

Where M is the mach number of a certain flow, V is the velocity of that flow, and a is the local speed of sound. In a shock tube, there are different mach numbers to consider. For example, there is the mach number of the initial normal shock wave, along with the mach number of the freestream flow behind the shock wave. The initial shock wave mach number was studied by

[17] and was determined to have the following relation in a monotonically convergent shock tube:

$$\frac{P_4}{P_1} = \frac{1}{g}\left(1 + \frac{2\gamma}{\gamma-1}(M_S^2 - 1)\right)\left(\left(1 + \frac{\gamma-1}{2}\right)\left(\left(\frac{2}{\gamma+1} * \frac{(M_S^2-1)}{M_S}\right)^{-1} g^{\frac{\gamma-1}{2\gamma}} - \frac{\gamma-1}{2}\right)^{-1}\right)^{\frac{2\gamma}{\gamma-1}} \quad (2)$$

Where M_s is the incident shock mach number, $\gamma$is the specific heat ratio of the gas, and P is pressure. Additionally, subscripts 1 and 4 reflect the respective regions the parameters take place. The parameter g is simply a function of area for a monotonically convergent shock tube, and its relation can be found in appendix A.

Similarly, for flow in a shock tube, the freestream mach number is determined by the following relation:

$$M_2 = \frac{\frac{2a_4}{\gamma+1} * \frac{M_S^2-1}{M_S}}{a_2} \quad (3)$$

With the subscript 2 also reflecting its respective region. It should be noted that the speed of sound in region 2 is a function of shock mach number and the temperature in region 1, which is atmospheric. Therefore, it can be seen that both mach numbers are solely determined by the pressure ratio of the driver and driven section, and the speed of sound of the respective regions. Since the area of the shock tube is fixed, it is not considered as a variable. However, since the boundary layer grows behind the shock wave, the effective area changes inside the shock tube slightly, and the mach number seen by theory is slightly overestimated. Therefore, the attenuated value of the mach numbers results in slightly different pressure ratios depending on the individual values of the pressures in region 4 and in region 1. Thus, the mach number should be found experimentally through various methods in order to know the conditions to generate a shock mach number with high accuracy.

Next, Reynolds number is an extremely important variable that dictates the behavior of many flows, including the flows inside a shock tube. The Reynolds number is the ratio of inertial forces to viscous forces and can aid in determining the theoretical transitional point of a flow from laminar to turbulent. The Reynolds number can be defined by the relationship below:

$$Re = \frac{\rho V d}{\mu} \tag{4}$$

Where Re is the Reynolds number, ρ is the density of the fluid, d is a reference length, and μ is the dynamic viscosity of the fluid. It should be noted that the reference length is typically defined by some length of a test article or the length of a boundary layer. The reference length for the following experiments will be the diameter of the liquid droplet inside the test section. For many test facilities, the unit Reynolds number is important as it can present the flow characteristics of many different applications by varying the length scale, and therefore illustrating the typical flow over different test articles. The unit Reynolds number can be defined as:

$$Re\ (1/m) = \frac{Re}{d} = \frac{\rho V}{\mu} \tag{5}$$

Since the Reynolds number depends on density, the pressures of region 1 and 4 can be varied to change the Reynolds number without changing the Mach number. Since both nondimensional numbers vary with velocity, this is not an ideal variable to change. Normal shock wave relations can be used to find the pressure in region 2 behind the shock wave, along with the temperature in region 2. After these parameters are found, the equation of state can be used to find the freestream density, and has the following form:

$$P = \rho R T \tag{6}$$

Where R is the specific gas constant of air, and T is the local absolute temperature. Finally, viscosity can be found utilizing Sutherland's Law, which has the following form:

$$\mu = \mu_{ref}\left(\frac{T}{T_{ref}}\right)^{1.5}\frac{S_u+T_{ref}}{S_u+T} \tag{7}$$

Where the ref refers to a reference value, where in this case are the values at a temperature of 273.15 K, and S_u is the Sutherland's constant, which for this case is 111 K [18]. There are also a couple more nondimensional numbers that are important when discussing the aero breakup of a liquid droplet. The first number which is more widely regarded as an important parameter, is the Weber number, which has the following relation:

$$We = \frac{\rho V^2 d}{\sigma} \tag{8}$$

Where We is the weber number and σ is the surface tension of a droplet in a moving fluid. For the case of water, the surface tension is found to be 72.8 mN/m. This value is fairly constant for different pressures and temperatures and will be treated as a constant. Similar to Reynolds number, the dependance on density and diameter make it impossible to change Weber number while keeping the Reynolds number the same if the test gas and droplet composition remains unchanged. However, the freestream Reynolds number can change while keeping the other 2 nondimensional numbers constant by changing density and the diameter of the droplet at an inversely proportional rate.

Finally, the other nondimensional number in which the aero droplet breakup is impacted is the Ohnesorge number, which is directly related to the Laplace number. While the Weber number characterizes the droplet breakup by its inertial characteristics, the Ohnesorge number characterizes the droplet breakup with its viscous characteristics and has the following relationship:

$$Oh = \frac{\mu_d}{\sqrt{(\rho_d d\sigma)}} \tag{9}$$

Where Oh is the Ohnesorge number and the subscript d denotes the property of the liquid droplet. It can be seen that the Ohnesorge number is made up of solely the liquid properties and can be changed if needed. The easiest way to change the Ohnesorge number is to change the liquid composition or diameter, although changing the temperature of the droplet can also change the characteristics of the Ohnesorge number. However [19] found that an Ohnesorge number below 0.1 will result in negligible viscous effects, leaving Weber number as the dominating parameter to impact the droplet breakup. Overall, understanding these 4 nondimensional numbers is quite important to analyze the aero breakup of a liquid droplet in a high-speed flow.

Chapter 2: Background

2.1: Literature Review

Testing liquid droplets in high-speed gaseous flows has been studied for nearly 80 years. Some of the earliest documentation investigating high speed flow interactions with liquid droplets stem from [20], which observes the effect of the Weber number of a liquid droplet and how a varied Weber number results in different types of fluid breakup. [20] found that there existed 5 different ranges of weber numbers that dictated how a fluid droplet would break down in a high-speed flow. These 5 regions are illustrated below:

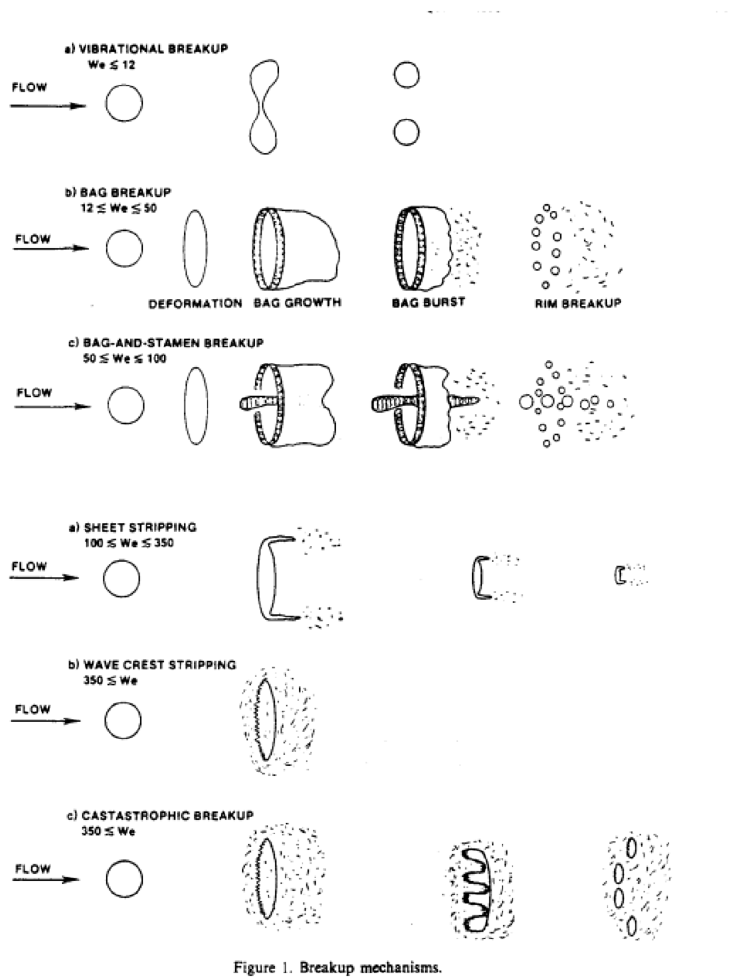

Figure 4: Different Breakup Modes of a Liquid Droplet for Different Weber Numbers

That is, the droplet's shape during the aero breakup is significantly affected by the Weber number of the experiment. For Weber numbers less than 12, the droplet has a vibrational breakup, meaning the droplet becomes vertically elongated until it splits into 2 droplets. When the Weber number exceeds 12 but remains less than 50, the water droplet experiences bag breakup, in which the droplet extends horizontally, and creates a concave hole almost like a paraboloid. Then, the downstream end of the bag bursts which causes instabilities in the droplet until the rim is broken up into small droplets. There are several other breakup modes between a Weber number of 50 and 350 that are not applicable to this experiment. After a Weber number of 350 is exceeded, the droplet undergoes catastrophic breakup, in which the droplet is atomized rather quickly, with only a relatively 2-D plate left that quickly breaks up into smaller droplets. This is a very useful condition, as the rapid atomization of the water droplets has many uses for fuel injection and combustion testing. Additionally, [21] discussed how water droplet breakup may differ from the previous finding in high-speed flow. They did so by employing a rarefied gas condition that allowed the authors to find the breakup characteristics for similar Weber numbers to previous experiments at much higher Mach numbers. From this, it was found that nonlinearities in the breakup were cause by multiwave penetration. This inspired [22] to investigate the aero breakup of a droplet at different mach numbers.

Considering the aerodynamic forces on a water droplet is of high importance, as the deformation of a droplet is applicable for fuel injection, characteristics of forces on an aircraft, and other reasons. The study on how to characterize the aerodynamic forces was presented by [23], and further reinforced by [22] for different Mach numbers. The relationship between the coefficient of the drag on the droplet is tightly related to the center of mass of the broken up droplet as a function of time. Although these resources consider the relationship for a spherical droplet, a relationship between the coefficient of drag and the center of mass as a function of time can be produced by following the procedure of [23] and use the area and volume of a sphere with a contact angle with a surface by using spherical coordinates. Then, new relationships can be made that also depend on the contact angle between the droplet and the surface.

Other authors talked about Rayleigh-Taylor Piercing and Shear Induced Entrainment

Recently, Guo et Al. analyzed the effects of high-speed flow on a wall attached droplet. Specifically, the effects of wall attachment angle between the droplet and a flat plate model were changed to examine the effect between surface wettability and the different breakup modes observed on a droplet aero breakup [24]. This is a very new topic, and Guo et Al. are the only authors to examine this condition for shock induced aero breakup of a droplet. Additionally, they also investigated the instability modes of the droplet and compared them with theory. Several other authors have used similar methods to find the instability modes of a coupled airflow-droplet condition [25].

Other researchers have investigated airflow breakup effects on wall-attached droplets. The previous studies on this topic have typically been at very low Weber numbers and Mach numbers. For example, [26,27] focus on wall laden droplet deformation and migration in low Weber number cases. [24] is the only study that has focused on higher Weber number and Mach number effects on a wall laden droplet, but their research does not focus on how the breakup changes under different conditions other than contact angle. Although it is an important topic for fuel injection applications, several other aspects of the experiment may also be useful to know. Some potential variables to change are the diameter of the droplet, along with the effect of different freestream conditions. Additionally, [24] analyzes the effects of a thin constant boundary layer, however analyzing the experiment on a shock tube wall can illustrate how a dynamically changing boundary layer can affect the results. It is important to conclude which condition leads to the ideal scenario for fuel injection purposes.

Overall, a study focusing on dynamically changing boundary layer could play a beneficial role in combustion applications. Comprehensive documentation of a time variant boundary layer interaction with a liquid droplet in high-speed flow has yet to be reported.

Additionally, the effect of a variable droplet diameter along with freestream unit Reynolds number is to be investigated to find how different conditions can affect the characteristics of the droplet breakup. Therefore, careful considerations will be implemented to discover these findings.

Chapter 3: Experimental Setup

3.1: Shock Tube dimensions/conditions

The following experiments were conducted in the transonic/supersonic shock tube at the University of Oklahoma High Speed Aerodynamics Lab. The driver tank is a 2 meters long cylinder with an 80 centimeter diameter. The tank is also designed to hold pressures of up to 1 Megapascal. Releasing the driver tank gas into the driven section is a pneumatic fast acting valve from ISTA Pneumatics. It is actuated from the high pressure, and as a result can actuate almost instantaneously. The fast-opening valve has a minimum operating pressure of about 500 kPa absolute in the driver tank so the valve can pneumatically actuate at a fast enough rate to avoid large disturbances in the flow. The fast-acting valve then feeds into the driven section, which is a 5 meters long rectangular tube with a 72x72 millimeter inner cross section. The interior corners of the driven section are also filleted with a radius of 4 millimeters. The driven section leads into the test section, which was designed and produced by [28], and its interior dimensions are designed to match the driven section geometry. The following diagram illustrates the setup of the shock tube used in this experiment:

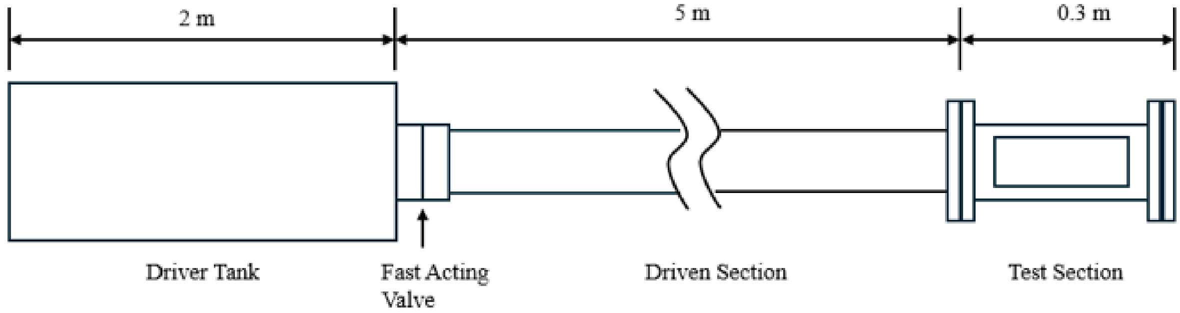

Figure 5: Diagram of High Speed Shock Tube used in the Experiment

A 6061 aluminum frame is the foundational structure of the test section for high strength and ease of manufacturing. The test section is 0.3 meters in length, but the initial shock wave only goes 254 millimeters past the driven section until it is reflected by the end wall. Acrylic windows were implemented for visualization, which show the side profile of the flow. The test section of the shock tube can be seen in the following figure:

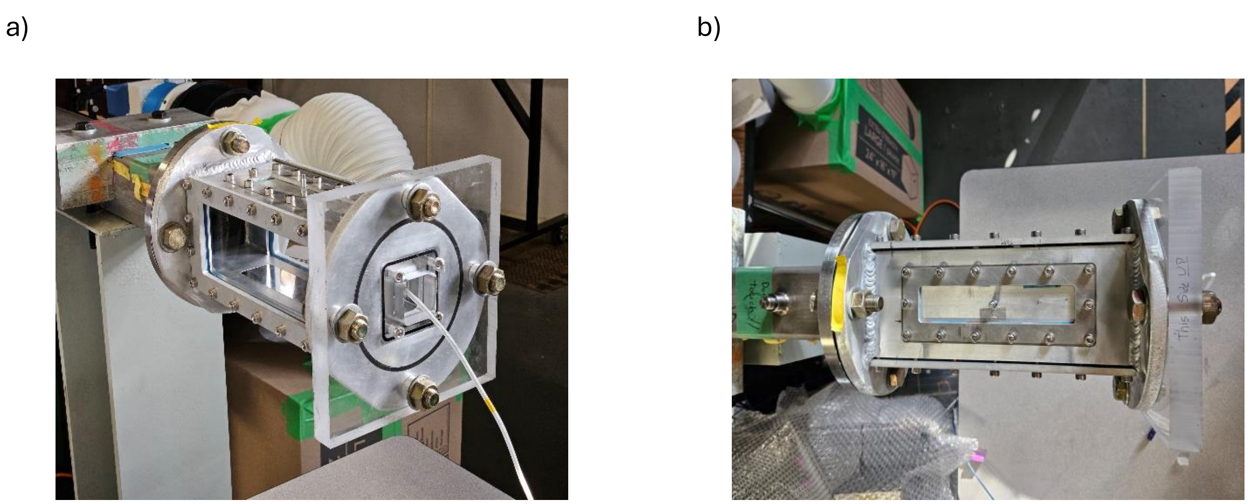

Figure 6: Installed Test Section for the shock tube in the High Speed Aerothermodynamics Laboratory from the a) Oblique side-back view and b) top view.

The shock tube test section has removable top and bottom plates so that different sensor locations and test models can be installed by the top and bottom walls. Additionally, the acrylic endwall is flush to the aluminum frame of the test section, allowing for a uniform reflected shock wave. Gasket material is employed to ensure proper sealing of the test section. For more information about the design of the test section, refer to [28]. Overall, understanding the characteristics of the shock tube is paramount to properly conduct shock tube experiments.

3.2: PCB Pressure Measurement

Pointwise pressure measurements were recorded with high sampling rate piezoelectric pressure sensors (PCB 113B28). A piezoelectric sensor measures the axial force seen by the face of the sensor and converts this force into voltage. The sensors sampled the pressure history of each experiment at a rate of 1 MHz. Additionally, in order to improve resolution of the recorded pressure, the input range of the measured voltage was slightly decreased from 5V to 2V to set the resolution to 0.02 V/mV. In order to properly measure the pressure with these sensors, they must be installed flush to the surface of the wall. For these experiments, 2 PCB sensors were used to measure the pressure in the test section at different times. The voltage recorded by the sensors were then sent to a data acquisition system known as Nitrogen from Dewetron. Additionally, a third PCB sensor was implemented as the furthest upstream sensor and used as a trigger to begin recording pressure data and high speed camera data. The data acquisition system used was Nitrogen, which is able to record the PCB signals at the impressively high 1 MHz sampling frequency. Therefore, once the shock wave passes the most upstream PCB, the sudden increase in voltage can be used as a triggering device telling the DAQ to save the recorded data for a specified period of time. More information on the triggering system for the Shadowgraph system will be discussed later. Figure 7 illustrates the relative location of each sensor for the experiments.

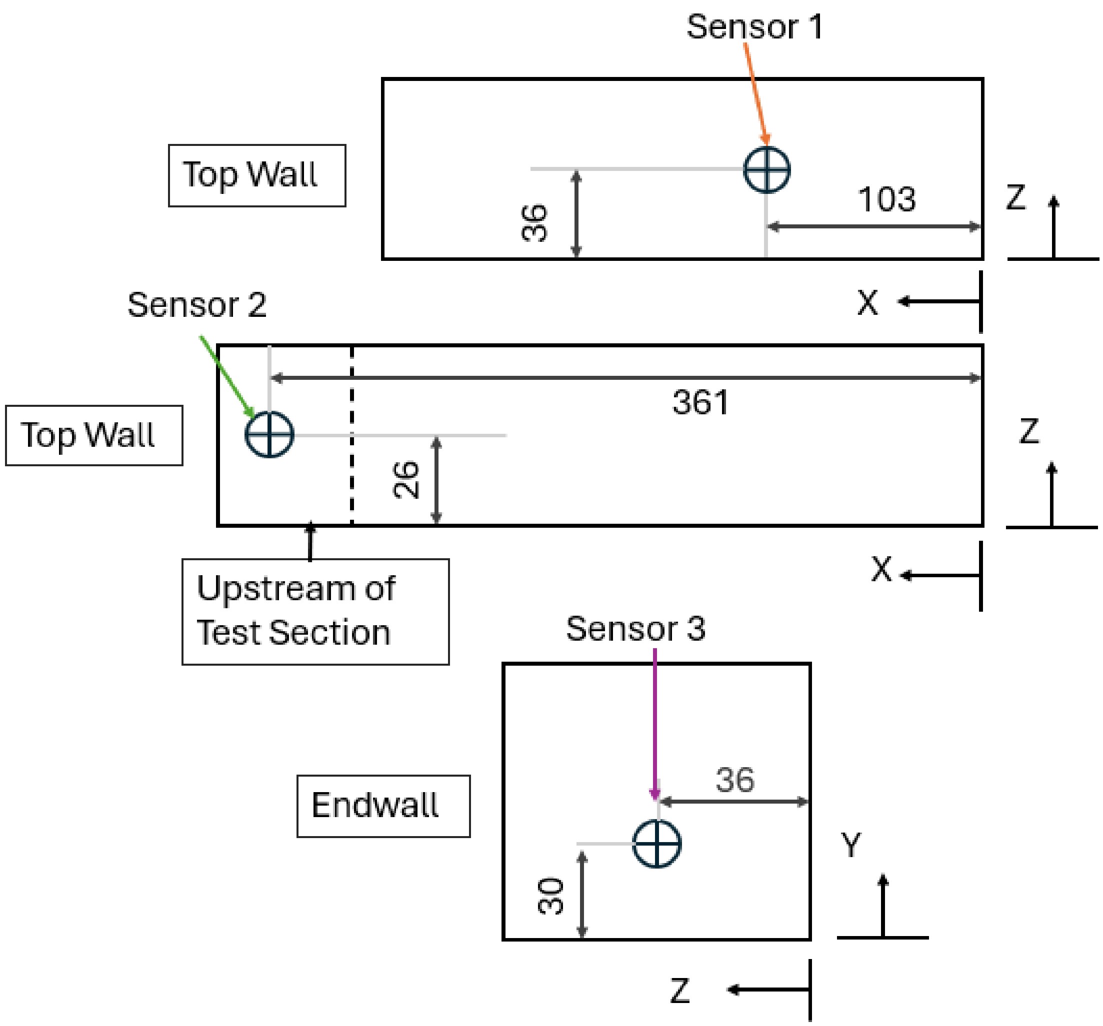

Figure 7: Locations of each PCB pressure sensor in the test section. X, Y, and Z denote the origin and the Axes in the test section respectively. All dimensions are in millimeters

From the diagram above, the pressure sensor layout can be defined, along with the origin. Two PCB pressure sensors were placed in the top wall upstream of where the droplet is placed. These two pressure sensors measure the static pressure field by the side wall of the test section. Sensor 1 is on the top wall of the test section, 103 mm from the endwall. It is near the center x and Z location on the top wall. Sensor 2 is placed upstream of the test section, 361 mm upstream of the endwall. It is in the center Z location in the driven section. Since the sensor is placed before the test section, the region by sensor 2 cannot be visualized. Additionally, Figure 2b illustrates the configuration of the location for each sensor on the top wall. On the other hand, Sensor 3 is placed in the endwall, where stagnation pressure is measured. It is placed in the center Z location, although it is slightly offset from the center Y direction. This is to allow the potential of a thermocouple mount in the center of the endwall, although a thermocouple was not employed for the following experiments. Nevertheless, these three sensors will be key to obtaining the freestream conditions.

It should be noted that each PCB pressure sensor was mounted flush with the surrounding wall. Therefore, no protruding bodies should affect the flow, and any resonating frequency caused by flow over a gap should be minimized as well.

3.3: Hydrophobic Coatings

To analyze the effect of droplet contact angle with the surface, two separate conditions were employed. The first hydrophobic coating that was used was Adam's Advanced Graphene Ceramic Compound, which allows aluminum to have an attachment angle of 110°. The coating was applied by first cleaning the plate that is placed inside the test section with denatured alcohol, and then dried with a chemical wipe. Afterwards, the Adam's coating is applied by pouring several drops into a microfiber cloth and rubbed in fairly vigorously into the plate. A water droplet on the Adam's Advanced Graphene Ceramic Coating can be seen below:

Figure 8:Water droplet on Adam's Graphene Ceramic Coating compound. The attachment angle on an aluminum surface is slightly greater than 90°.

However, to contrast with the other hydrophobic condition, after several days of application, the compound was slightly removed with denatured alcohol, which reduced some of the hydrophobic properties. The final attachment angle was found to vary between 70° and 80°, which reflects aluminum properties quite closely. Figure 9 illustrates how a droplet looks for this condition:

Figure 9: Water droplet on non-hydrophobic surface. The attachment angle on an aluminum surface is slightly less than 80°

The droplet produced by this condition allows for a low contact angle to compare to the very hydrophobic surface which will allow for more general observations for the difference in flow structures between the two cases. For the other surface to be evaluated, Rustoleum NeverWet Multisurface water repellent was applied to the other half of the plate. The Rustoleum NeverWet treatment comes with two coatings: a base coat and a top coat. The base coat provides a consistent roughness element while decreasing the surface free energy (SFE), which allows for an increase in the hydrophobicity of the treatment. The top coat then deposits silicon-based nanoparticles homogeneously contained in a gel-like substance. After the top coat is cured, the gel-like substance is vaporized, the silicon-based nanoparticles are neatly deposited onto the surface of the base coat, a unique surface morphology to promote trapped air particles below the water droplets that increase the surface tension within the droplets [28]. Therefore, a brief study was conducted that quantified the effectiveness of each coating based off how many layers of the coating was applied. That is, the hydrophobicity of the material was related with how many layers on the surface are. This was done for the base coat and the top coat.

On a test plate, the relationship between the layers of the base coat and the hydrophobicity was tested first. The test plate was cleaned with denatured alcohol and then dried with a chemical wipe, just like with the plate for the test section. Afterwards, the plate was sectioned with tape, so that overlapping of the coating for each test was not an issue. Then, the base coat was applied roughly 9-12 inches away from the plate and passed over each section of the plate with a singular pass. After waiting 30 minutes, which is the cure time for the base coat, the second and third section had a second coat applied. Finally, after another 30 minutes, the third section had a third coat applied. After all three sections were fully cured, 2 layers of the top coating were applied to all 3 sections. The droplet contact angle between the droplet and the surface was then measured with photo imagery. The angle was found by finding the inverse tangent of the initial slope from the attachment point between the droplet and the surface. A similar process was done with the top coat. First, 2 layers of the base coat were applied appropriately. Then, the top coat was applied like how the base coat tests were applied, but instead of increasing the layers by increments of 1 layer, the layers of the top coat were applied by increments of 2 layers. Examples of these droplets are visualized in Figure 6.

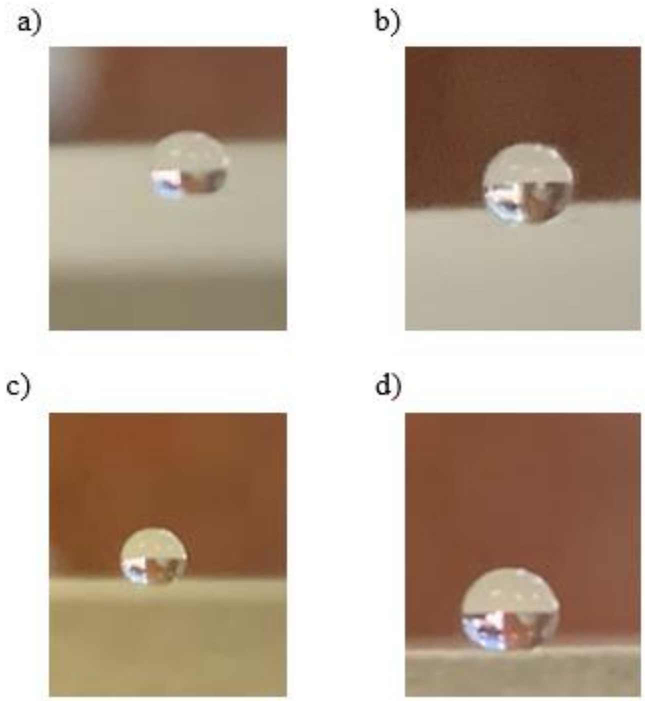

Figure 10: Droplet characterization for small droplets at a) 1 base coat and 2 top coats, b) 3 base coats and 2 top coats, c) 2 base coats and 1 top coat, d) 2 base coats and 5 top coats

Figure 10 illustrates how the droplet changes with a different amount of layers of the hydrophobic surface compound sprays. Figures a and b show the minimum and maximum tests for the effect of the base layer coating, while figures c and d show the minimum and maximum tests for the effect of the top layer coating. After finding the slope of the attachment point, the effects of the coating thickness and droplet contact angle were found and are reflected in the figures below:

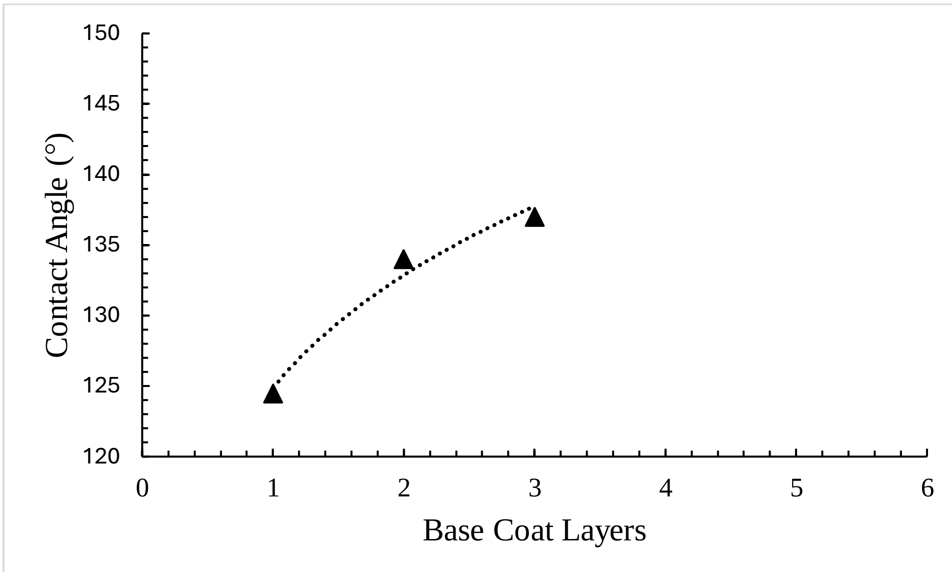

Figure 11: Relationship between number of base coat layers and attachment angle for water droplet

3 millimeter droplets were placed on an aluminum surface in which different layers of the base coat were analyzed. The base coat then had two layers of the top coat to investigate the total hydrophobicity of the droplets. It is illustrated that the attachment angle of the water droplet improves as the thickness of the base coat increases. Therefore, applying several base coat layers to increase the thickness is necessary to achieve good conditions inside the test section. It should be noted that the rate at which the contact angle decreases with the increasing thickness of the base coat. This is a result of the fundamental properties of surface free energy, in which can only increase the hydrophobicity of a droplet by about 50% due to the Young-Dupre equation [30]. This means the hydrophobic properties produced by the base coat reaches a maximum value after

a certain number of additions, after the surface free energy reaches some constant value. Additionally, the relationship between the top coat thickness and wettability of the surface was briefly studied, and the results can be seen in the figure below:

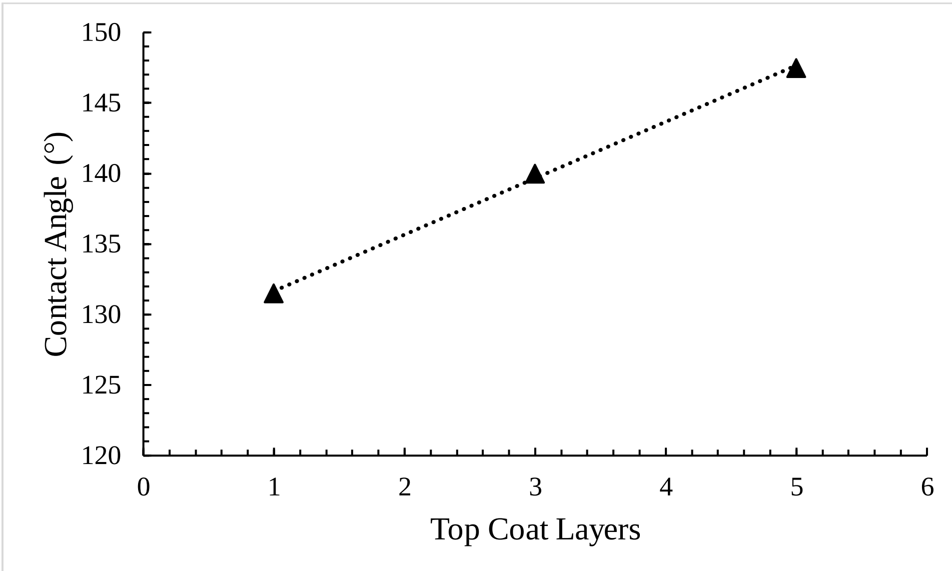

Figure 12: Relationship between number of top coat layers and attachment angle for water droplet

In the case of figure 12, 3 millimeter droplets were placed on 3 different conditions again. At first, 2 layers of the base coat were applied, and afterwards a variable number of top coats were applied. Contrary to the base coat thickness influence, the wettability of the surface is linearly related to the number of top coat layers. It should be noted that unlike the base coat, the thickness of the top coatings do not seem to reduce the effectiveness of the next layer. This is because unlike surface free energy, changing the surface morphology of a surface has been found to achieve attachment angles of over 160° [29]. Therefore, changing the surface morphology by layering areas of nanoparticles results in an increase of air pockets maintaining the surface tension of the water. Although it is linear for up to 5 coats, it should be expected that at some point the top coat thickness variation also result in some maximum value, as it is mathematically constrained at 180°, and physically constrained by slightly less than 180°. Thus, it should be emphasized to apply many layers of the top coat in order to produce the best condition for the experiment.

Before the application of the Rustoleum Neverwet coating, tape was used to cover the other half of the plate already covered with the Adam's coating. Tape was also used to cover the gasket material around the plate. Afterwards, the base coats and top coats were applied by Dr. Hiroshi Ozawa, in which a rigorous amount of both coatings was applied. The final contact angle produced by the Rustoleum Neverwet coating is about 133-140°. As a result, the difference in contact angles between the two conditions is over 50°, and any differences caused by the contact angle of the droplet should be sufficiently documented. The test plate with both the hydrophobic surface and non-hydrophobic surface is visualized below:

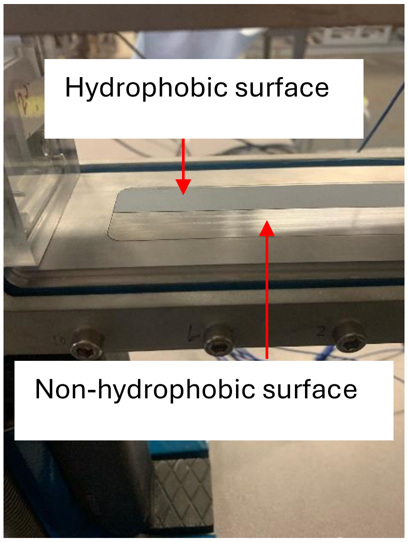

Figure 13: Test plate with different hydrophobic properties installed into the shock tube. The hydrophobic surface has an attachment angle of about 135°, while the non-hydrophobic surface has an attachment angle of about 80°.

Figure 13 illustrates how the different hydrophobic properties were obtained for each test. Since the different material is in the spanwise direction, downstream properties should not vary between the two conditions, as cross-stream effects are minimal and 1-dimensional flow can be estimated.

3.4: Inserting Droplets

For consistent droplet placement between each test, an 5 mm clearance hole was made in the top plate of the test section 80 mm away from the endwall so that a hypodermic needle attached to a syringe could accurately place a consistent droplet at a consistent location. Deionized water was used as the liquid in order to maintain a constant purity level to remove the variable of impurity composition for attachment angle and droplet breakup characteristics. Due to the high specific heat of water, the density of the water will be considered as 998 kg/m^3, the viscosity is taken as 0.001 $N*s/m^2$, and the surface tension is 72.8 mN/m. A depiction of the method in which the liquid droplets were inserted can be visualized below:

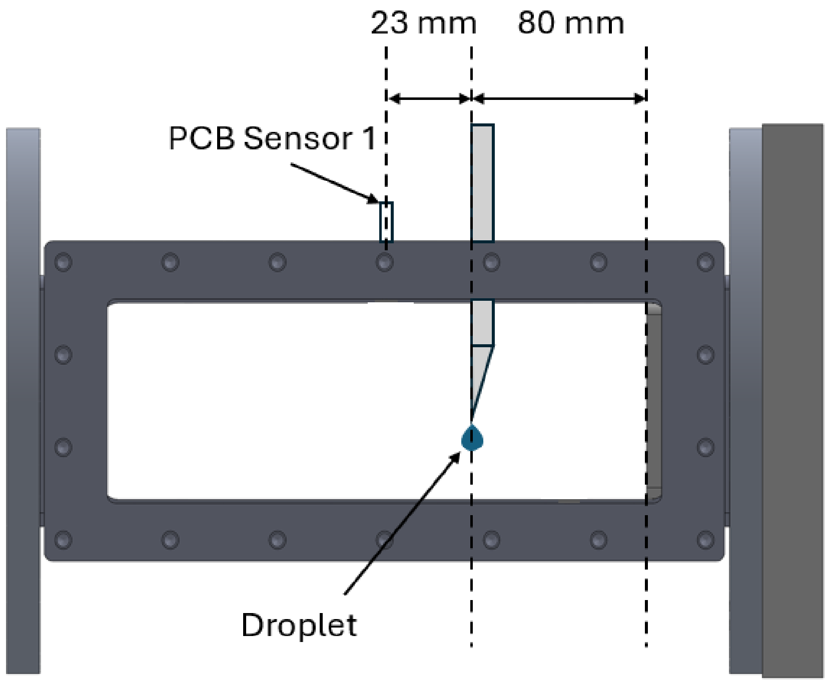

Figure 14: Illustration of How Droplets were Inserted into the Test Section

The droplets were inserted into the test section, with camera pixel measurements to ensure the location of the droplet and dimensions of the droplet were roughly consistent. Additionally, in order to properly analyze the droplets, some key definitions for different variables are gathered from [30] and reproduced for both the hydrophobic and non-hydrophobic droplets. These variables are illustrated as follows:

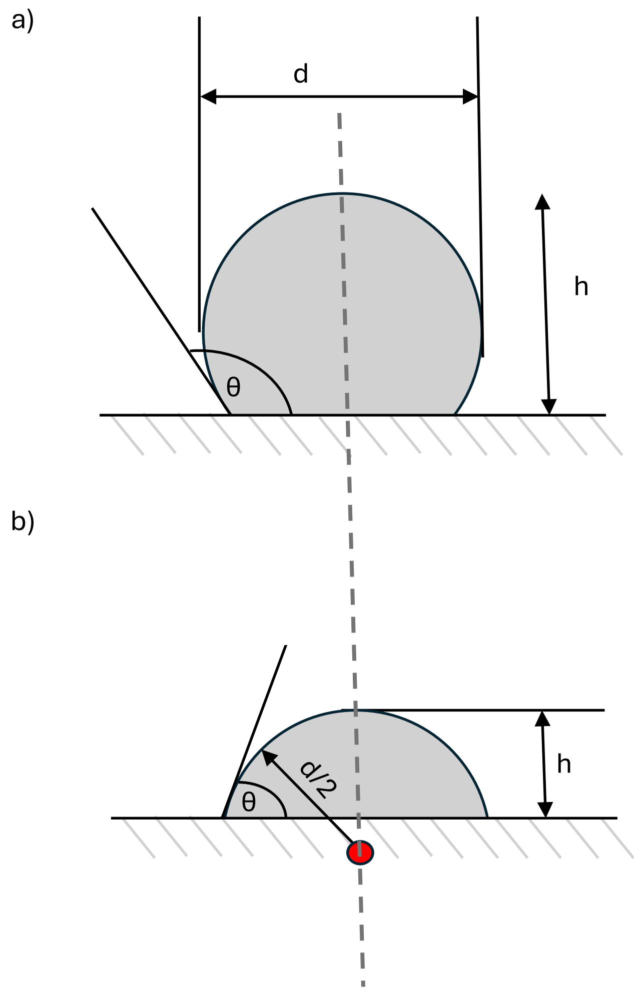

Figure 15: Variable definitions for droplet diameter, attachment angle, and droplet height for a) hydrophobic droplet and b) non-hydrophobic droplet

Figure 15 depicts how different variables are defined for the experiment. One of the most important variables to be studied is the attachment angle of the droplet. The attachment angle θ is defined by the initial slope of the droplet when it meets the surface. It can be seen that a fully spherical droplet would have an attachment angle of 180°, while a flat puddle of water would have an attachment angle near 0°. Although neither are possible to produce on a flat surface, different attachment angles can be produced by changing the properties of the surface mentioned earlier. Additionally, the diameter of the droplet for a droplet on a hydrophobic surface is defined by the maximum horizontal distance found between the edges of the droplet, and is shown in figure a. On the other hand, for a droplet on the non-hydrophobic surface, the maximum horizontal distance is identified by the region where the droplet meets the surface. Therefore, the actual diameter of the droplet must be defined. From the Young-Laplace relationship, which is utilized in [24], the radius of curvature can be defined as the droplet's actual radius for a water droplet. Thus, the diameter of the droplet can be calculated by doubling the value of the radius of curvature. It should also be noted that in this research, the length scale found by doubling the radius of curvature will simply be referred to as the droplet diameter for convenience. However, it should be acknowledged that a more correct term to be implemented should be diameter of curvature, as the interactions with the wall preventing the droplet from being spherical do not fully match the definition of a diameter.

3.5: Shadowgraph setup

In order to properly analyze the high pressure flow-droplet interaction, a Z-type shadowgraph setup was employed. The camera used was a Photron FastCam Mini AX 100, recording at a sampling rate of 61200 frames per second with a field of view of 256x128 pixels. The shutter speed was 2.48 microseconds. This shutter speed allows a rough visualization of the incident shock wave and other flow characteristics, while still having enough brightness to visualize the dynamics of the droplet aero breakup. The diagram reflected in Figure 16 properly illustrates the Shadowgraph setup.

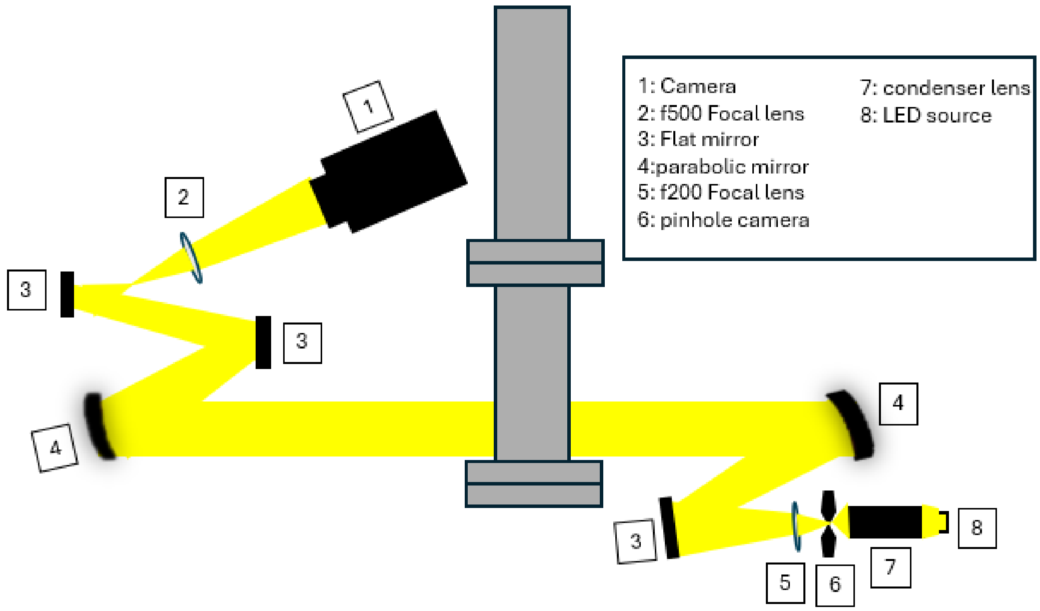

Figure 16: Shadowgraph Schematic to illustrate the method of capturing high speed videos. Schematic reflects the X-Z plane.

The LED sends out a light beam that goes through a condenser lens and a pinhole camera, then sent through an f200 focal lens. Afterwards, a flat mirror reflects the beam into a concave mirror which results in a parallel beam of light through the test section onto another concave mirror, which condenses the image. This beam is then reflected onto 2 more flat mirrors, and then the beam is sent through an f500 lens to increase the focal length of the beam. Finally, the camera views the focused image of this optical setup. Since no knife edge is applied to cut some of the light disturbances at the focal point, it is considered shadowgraph photography, which visualizes the second density gradient of a flow. As a result, flow phenomena such as the incident shockwave and boundary layers can still be visualized, but they will be fairly weak and not well defined. Nevertheless, the output camera data was recorded utilizing the complementary PFV4 software associated with Photron.

The pixel dimensions were first characterized by taking a reference image of the setup (a hypodermic needle which had a known diameter of 1.2 mm, which was verified with calipers). The reference image concluded that the pixel size in each test was 60x60 micrometers, as the reference images resulted in the needle being 20 mm in diameter. As a result, over 1300 pixels make up a droplet that is 2.48 mm in size, which is the minimum diameter utilized in the experiment. Therefore, this resolution should suffice to produce quality analysis of the post wave-droplet interaction.

When each condition in the shock tube is ran, it is important to set up a system to which the camera will record the flow that occurs in the shock tube while minimizing the amount of recorded data that is seen by the camera. This can be done by implementing a trigger. The Nitrogen DAQ that is utilized to record the pressure signals from the PCB signals can also output a digital signal. Therefore, once a shock wave passes the most upstream pressure sensor, a signal can be sent to a function generator to produce a TTL signal. This step signal will then tell the FastCam to begin recording, and it will continue recording until a maximum number of frames are recorded. The maximum number of frames that are recorded can be set with the PFV software. It is then important to reset the function generator so that a new TTL signal can be produced for the next experiment.

The region of interest, or field of view, of the visualization area was decided by running a test at full resolution and visualizing the distances travelled by the droplet. Knowing the minimum droplet diameter being just over 40 pixels in diameter, finding the necessary width and height of the visualization area was conducted by finding the number of pixels travelled by the droplet during the duration of the experiment. The width and height of the visualization area is 15.36 x 7.68 mm respectively.

In order to identify the deformation of the droplet for each condition, the shadowgraph data was analyzed in MATLAB. The deformation was tracked by utilizing edge detection on the figure throughout the time of the droplet breakup. This was conducted by using the Canny method, which is a method of edge detection, and can aid in tracking the deforming droplet. It works by finding the first spatial derivative between the pixels, and if it exceeds a threshold, then it marks it as a hard edge. Additionally, if it passes a soft threshold, but not a large threshold, it is marked as a soft edge. Hard edges are saved as a binary 1, and soft edges are saved as 1 if they are adjacent to a hard edge. Soft edges are saved as 0 if they are not adjacent to a hard edge [31]. The thresholds chosen in this case were 0.05 to 0.2. It was found that the high threshold removed a lot of the noise around the droplet while the low threshold aided in keeping the droplet a continuous edge. One example is that the time history for the condition of a droplet that is 4.36 mm, a unit Reynolds number of $8.4*10^6$, and an attachment angle of 135° was found with raw image data:

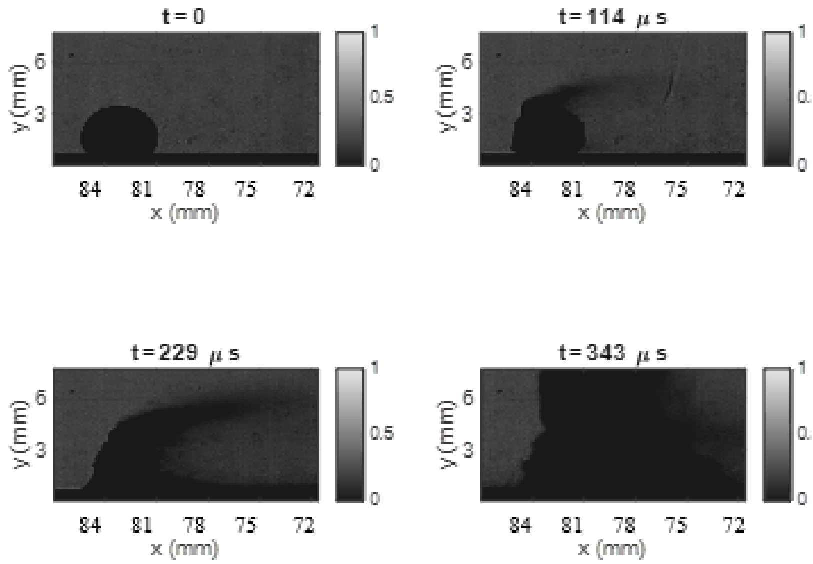

Figure 17: Raw Image Data for a droplet that is 4.36 mm, a unit Reynolds number of 8.4×10^{6} 1/m, and 135°

The breakup of the droplet is visualized, but the intensity profile between the broken up droplet and the rest of the image is not clear. Therefore, implementation of the Canny method allows for easy tracking of the droplet edge and how it deforms. The Canny method of the same time histories is visualized in the below figure:

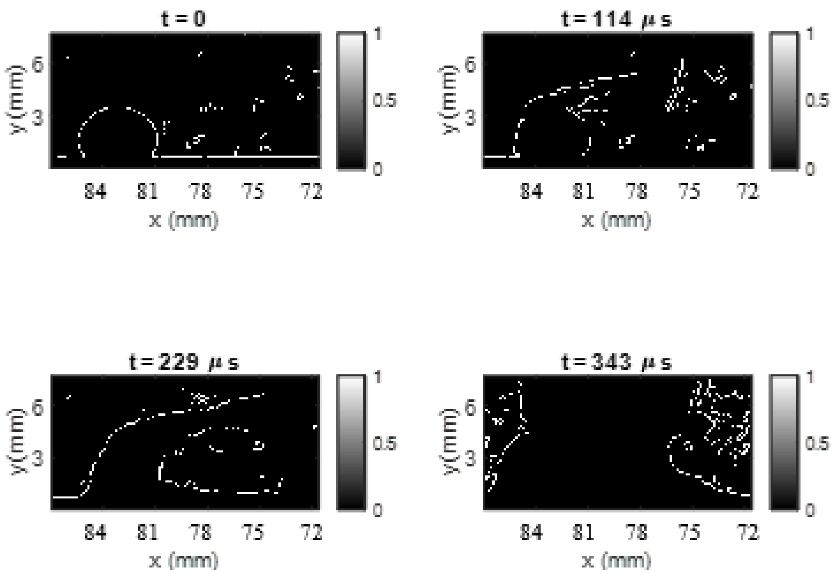

Figure 18: Canny Method Application for Shadowgraph of a 4.36 mm droplet with an attachment angle of 135° and a unit Reynolds number of 8.4×10^6 1/m

Although there are small interruptions in some of the edges, the general shape of the edge can be realized with this image processing technique. From here, displacement, change in width and height, and instability wavelengths can be estimated. These are measured by finding the changes in pixels between different conditions and converting the distance from pixels to a length scale such as millimeters.

3.5: Testing Conditions

In order to compare the effect of different conditions, it is important to get conditions in which the Reynolds number and weber number are constant, even in different conditions. If this is the case, then the effect of changing conditions (for example, freestream unit Reynolds number), can be identified and not conflated with other changing conditions. However, to successfully do this, the only parameters that can be changed that also won't change Mach number is the density of the freestream gas along with the diameter of the droplet. If the density is decreased by some arbitrary value, the diameter of the droplet must increase by the same arbitrary value as well. With the decreased density, the effect of changing freestream unit Reynolds number on the droplet breakup can be visualized.

The conditions in which the experiments were conducted in the shock tube, along with many of the freestream parameters, can be seen in the table below:

Table 1: Experimental Test Conditions in the Shock Tube

Condition	P_4 (kPa)	P_1 (kPa)	D (mm)	H (mm)	θ (°)	M_s	Re	Unit Re (1/m) (10^6)	We
1	502.9	9.4	2.70	1.92	129	1.98	13545	5.02	2090
2	499.1	9.6	2.76	1.14	76	1.96	13876	4.99	2061
3	590.3	12.1	2.82	2.06	133	1.98	18174	6.44	2783
4	590.9	12.1	2.82	1.30	75	1.99	18473	6.45	2883
5	699.8	16.1	2.70	2.00	134	1.96	22564	8.42	3373
6	699.2	16.1	2.70	1.39	78	1.95	22603	8.37	3341
7	501.7	9.4	3.32	2.36	129	2.03	17667	5.34	2924
8	501.5	9.4	3.52	1.29	73	2.01	18150	5.26	2882
9	591.5	12.2	3.42	2.44	134	1.97	21986	6.43	3321
10	591.5	12.2	3.42	1.26	75	1.99	22667	6.62	3539
11	700.8	16.2	3.42	2.30	131	1.95	28597	8.36	4210
12	699.3	16.3	3.54	1.42	78	1.95	30208	8.39	4429
13	501.5	9.3	4.36	2.84	133	1.96	21147	4.84	3174
14	501.8	9.3	4.42	2.1	85	1.97	21810	4.93	3328

15	591.4	12.2	4.22	2.69	135	2.00	28258	6.69	4475
16	591.4	12.2	4.22	2.1	85	1.99	27987	6.63	4372
17	700.5	16.3	4.24	2.82	134	2.00	37314	8.82	5878
18	699.9	16.3	4.42	2.1	82	1.96	37793	8.55	5673

These conditions were chosen for what should be investigated on this topic. Specifically, one of the primary parameters to be studied is the attachment angle of the droplet. In addition to changing the attachment angle, freestream unit Reynolds number is a notable parameter of investigation, as it has very important uses. For example, a ramjet inlet changing altitude but keeping a constant Mach number may want to know how their fuel efficiency changes. Thus, the effect of freestream unit Reynolds number should be investigated. However, because of its close relationship with weber number, there must be several tests related to changing the diameter by the same amount as the change in density. This way, the unit Reynolds number can be compared between constant weber numbers as well. Thus, the experiments were first organized by attachment angle (oscillating between a hydrophobic and non- hydrophobic surface between every test). Then, the droplet size remains constant, and unit Reynolds number is changed. Once the three unit Reynolds numbers are recorded, the diameter is changed, and the other two parameters are investigated again. It is important to know that each condition was tested 3 times to ensure repeatability and to characterize the accuracy and uncertainty of the experiment. Therefore, the values presented for each experiment are the average of the three recorded parameters for each condition.

Chapter 4: Results

4.1: PCB results

The 18 aforementioned conditions were conducted in the shock tube, with piezoelectric pressure signals recorded from the PCB sensors. The voltage data recorded from the sensors were then converted to pressure using a linear calibration coefficient for each sensor provided by Piezotronics and analyzed using MATLAB software. Since the PCB sensor only records impulses in pressure before stabilizing, the initial value must be offset to the known value of pressure in region 1. Additionally, the time scale for the sake of these experiments is offset to begin at the arrival of the incident normal shockwave at Sensor 103 mm from the endwall. The final pressure history for the two PCB sensors used for analysis can be seen in Figure 19.

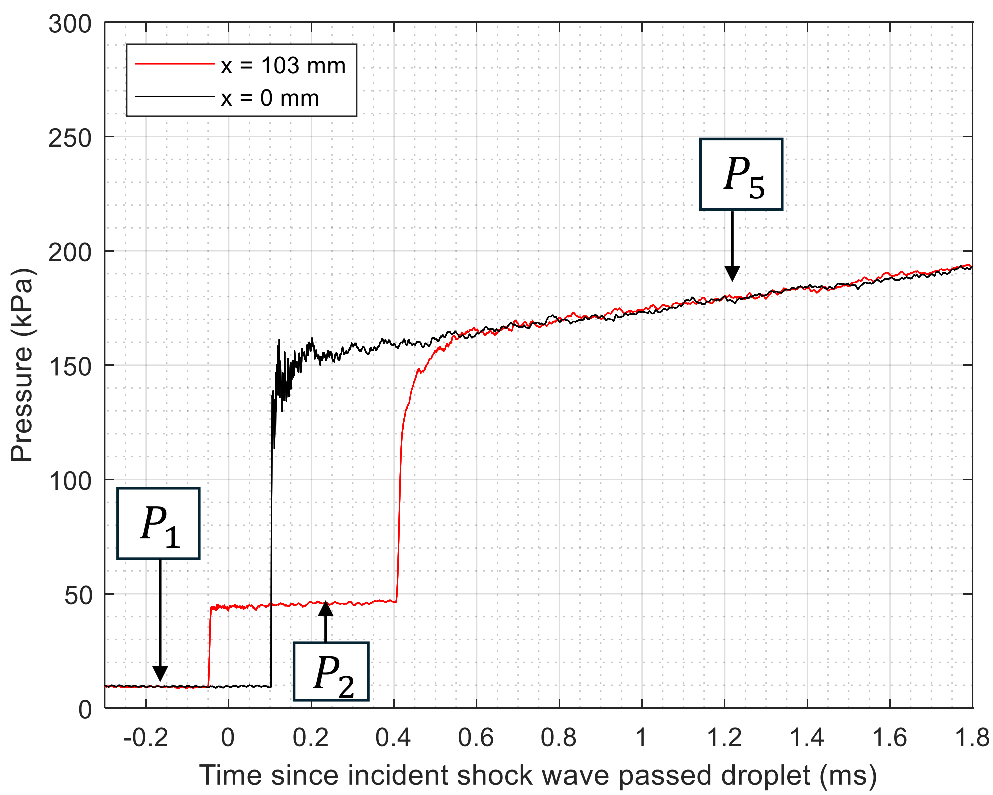

Figure 19: Annotated Pointwise Pressure Measurements for a Typical Shock Tube Experiment Illustrating the Incident and Reflected Shockwaves.

It should be noted that since the most upstream sensor (362 mm from the endwall) is used for the trigger in both the PCB data and the camera data, the data recorded by that is slightly altered and will be ignored for the point of analysis. Figure 14 depicts the impulse like change in pressure that is first caused by a normal incident shockwave, and then caused by the reflected normal shock wave. Specifically, these pressure values were recorded from condition 1, where unit Re = 5.0×10^6 1/m, P_4 = 500 kPa, and P_1 = 9.4 kPa. Typical analysis is determined from what the goal of the experiment is. For this case, the main area of analysis is the pressure in region 2, as that is when the breakup of the droplet is of highest importance. As a result, most of the analysis for this pressure data will be in region 2. There exist three important parameters that were previously unknown that can be obtained directly from the pressure history without applying any theoretical equations. First, the shock speed of the initial normal shock wave can be found from the initial impulse pressure rise from both locations documented. The fundamental principle of what is happening in the shock tube is reflected by the initial peaks. Specifically, the initial shock wave is seen to pass by the upstream pressure sensor 103 mm from the endwall by the initial pressure peak, and the pressure behind the shock wave increases to the respective pressure in region 2. Then, the initial shockwave is seen hitting the endwall after a certain amount of time, which increases the respective pressure all the way to the pressure found in region 5. It is important to find the time between the two impulse pressure peaks, and then apply the known distance between the two sensors. The shock speed can then be found by understanding velocity is distance divided by time. It should be noted that the speed calculated with this method has a slight error, as the flush surface of the PCB sensor has a diameter of 5.5

millimeters. However, since one of the sensors are flush with the endwall, the only uncertainty caused by this error is on the sensor 103 mm from the endwall. Thus, the true distance from the endwall is 103 ± 2.5 mm.

Furthermore, the pressure in region two can also be found, either as an average value or a function of time. The respective regions are labeled for the pressure history. The pressure in region 2 serves several purposes, such as finding the theoretical mach number of the incident shock wave, which can be compared to the mach number of the incident shock wave derived from the shock speed which is found by the pressure data. Finally, the last parameter found from the pressure history is the speed of the reflected shockwave. Similar to finding the initial shock speed, the time found between the initial pressure impulse at the endwall, and the second pressure impulse at the sensor 103 mm from the endwall is the time corresponding to the passage of the reflected shockwave. Since the distance is the same, the speed of the reflected normal shockwave can be found by distance over time.

These parameters are all extremely important to do any further analysis. For example, after finding the initial shock speed from the pressure data, other freestream parameters in region 2 can be found by employing normal shock theory, as the only variables that are required to know are the parameters in region 1 and the initial shock mach number. Additionally, understanding the initial shock speed and the speed of the reflected shock wave is key for designing the experiment. For example, when implementing the liquid droplet into the test section, it is important to know how long the droplet will be in the test section after the initial shock wave but before the reflected shockwave. This is because for other methods of data analysis, such as high speed camera imaging, knowing what framerate is needed or any other important parameters similar to that are dictated by the time in region 2. Thus, finding these parameters is fundamental for further analysis of any experiment.

Since each condition was conducted three times, the data must be averaged to find the overall behavior at each condition. It is also important to conduct the analysis mentioned previously not only to characterize the freestream conditions, but also to confirm the temporal stability of regions 1 and 2 to ensure the freestream conditions are unaffected by the presence of a small water droplet. The average pressure signals recorded by the sensor 103 mm from the endwall for every tested unit Reynolds number and diameter can be seen in the figure below:

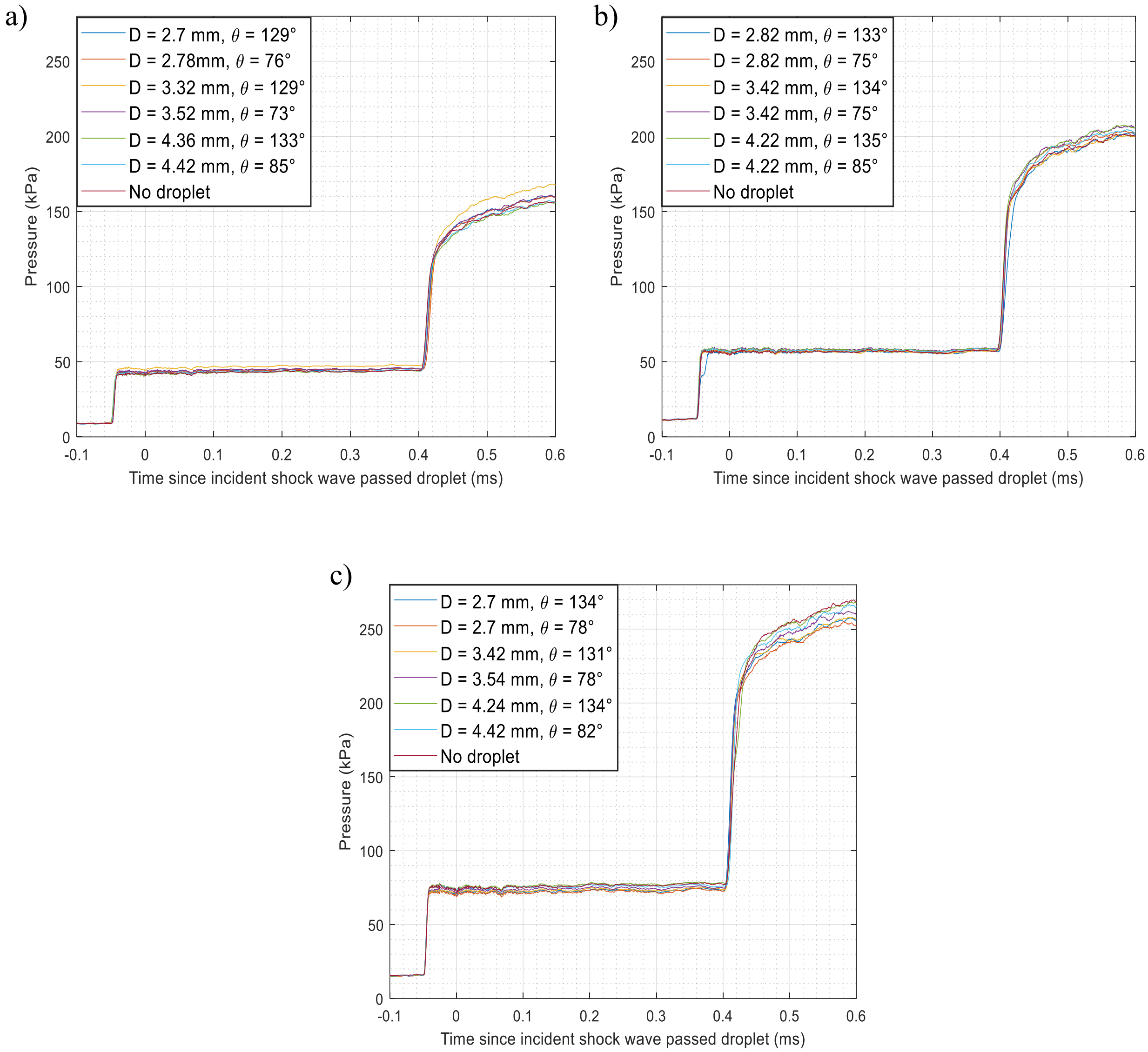

Figure 20: Pressure History recorded 103 mm from the endwall with different diameter droplets in the test section at a) $Re = 5.0\times10^6$ 1/m b) $Re = 6.4\times10^6$ 1/m and c) $Re = 8.2\times10^6$ 1/m

Figure 20a reflects conditions 1,2, 7, 8, 13, and 14. Figure 20b reflects conditions 3, 4, 9, 10, 15, 16, and Figure 20c illustrates conditions 5, 6, 11, 12, and 17, 18. The pressure recorded is on the top wall 103 mm away from the end wall. It is evident that the presence of any size droplet has almost no impact on the freestream pressure time history seen by the pointwise pressure sensors. This is reflected in that the no droplet case almost perfectly matches every other case, and slight differences are attributed to small variations in the test conditions. Additionally, it is important to ensure that the pressure history recorded by the sensor at the endwall is also in good condition. Since this sensor is downstream of the liquid droplet, it is possible that some additional variations would appear in the sensor's signal. The pressure history recorded by the PCB sensor that is flush to the endwall can be seen in the figure below:

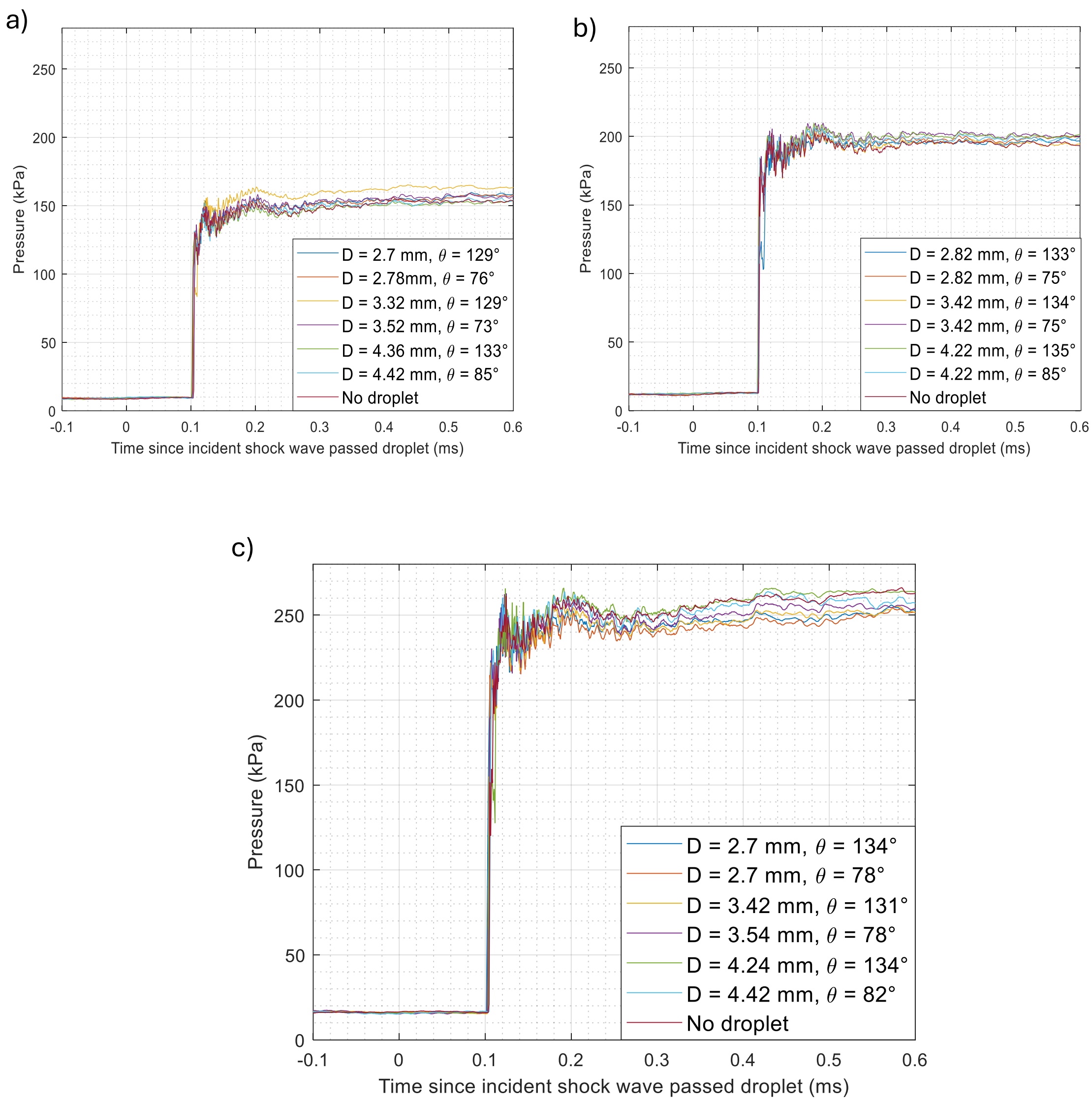

Figure 21: Pointwise Pressure History recorded at the endwall with different diameter droplets in the test section at a) $Re = 5.0\times10^{6}$ 1/m b) $Re = 6.4\times10^{6}$ 1/m and c) $Re = 8.2\times10^{6}$ 1/m

Figure 21a reflects conditions 1,2, 7, 8, 13, and 14. Figure 21b reflects conditions 3, 4, 9, 10, 15, 16, and Figure 21c illustrates conditions 5, 6, 11, 12, and 17, 18. The pressure recorded was at the endwall perpendicular to the flow. Similar to the pressure histories found at the sidewall 103 mm from the endwall, the pressure at the endwall experienced minimal disturbances caused by the presence of a water droplet. This can be concluded as the no droplet case is quite similar to the other conditions in region 1 and 5. The pressure in region 5 can also be found from Figure 9, as it remains relatively constant after a few hundred microseconds. It is found that even with normalized pressure, the presence of the droplet does not affect the freestream parameters, confirming further testing can successfully be completed without considering the presence of the droplet.

Overall, the pressure data reflects that the presence of a liquid droplet inside a monotonic convergent shock tube has minimal change in the freestream conditions and reflected conditions inside the shock tube. This trend has very little variation with diameter or freestream Reynolds number. Therefore, the PCB pressure data can be a useful tool to determine many of the parameters that will aid in analyzing additional phenomena in the post wave flow interactions with a liquid droplet.

4.2: Shadowgraph Results

Although the PCB data can depict the extent of which a liquid droplet impacts the freestream conditions behind a shockwave in a shock tube, it does not detail how a droplet breaks up under a high pressure flow behind a shock wave. Therefore, it is important to use high speed imaging to find the evolution of the droplet breakup in a high speed flow. The images of the aerobreakup of a wall-laden liquid droplet were obtained with the shadowgraph setup and high speed camera for each condition. Thus, 54 total series of images detailing the characteristic breakup of a wall-laden droplet were obtained with the shadowgraph setup. The evolution of the droplet breakup with shadowgraph imagery is captured, with roughly 22 frames in region 2 detailing how the droplet breaks up. The deformation of a hydrophobic droplet with an attachment angle of 129°, diameter of 2.7 mm, and freestream Reynolds number of 5.0×10^{6} 1/m can be seen in the figure below:

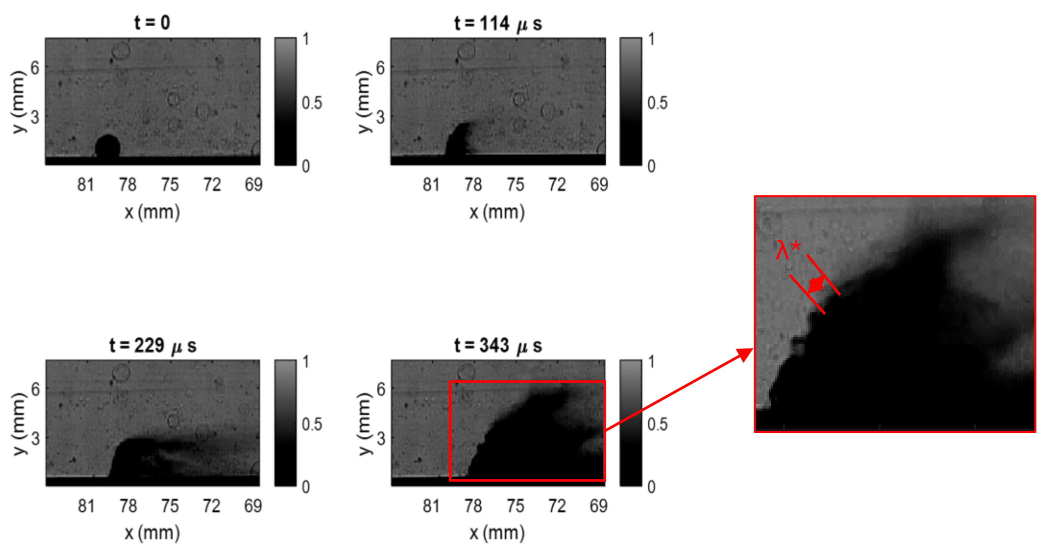

Figure 22: Time Progression of a Hydrophobic droplet with a Diameter of 2.7 mm and unit Reynolds number of 5.0×10^{6} 1/m with the total breakup zoomed for instability visualization

The condition for these series of images is condition 1. Figure 22 illustrates some common behaviors found in previous research. After t = 0, the shockwave passes the droplet from left to right towards the end wall. Then, 100 microseconds later, the droplet begins to breakup towards the top surface and towards the downstream bottom side of the droplet. After just over 200 microseconds, the droplet then continues the breakup, with a flattening of the curvature of the upstream side of the droplet, almost to a linear curve. Instabilities can be seen to start development at this point. Finally, after 340 microseconds, the droplet is significantly broken up, with fairly significant instability wavelengths seen on the upstream side of the droplet. The average wavelength for this condition was about 6 pixels. Analysis over the wavelengths between each condition will be conducted later. Additionally, the droplet can be seen to travel downstream as time progresses, which is a result of the drag force. The drag force can be estimated by the distance travelled by the droplet.

Similar to the previous condition, a droplet in the same freestream unit Reynolds number and diameter (diameter of 2.7 mm, unit Reynolds number of 5.0×10^{6}), but at a leading edge attachment angle of 72° is tested. The time history of the aforementioned condition can be illustrated by the following figure:

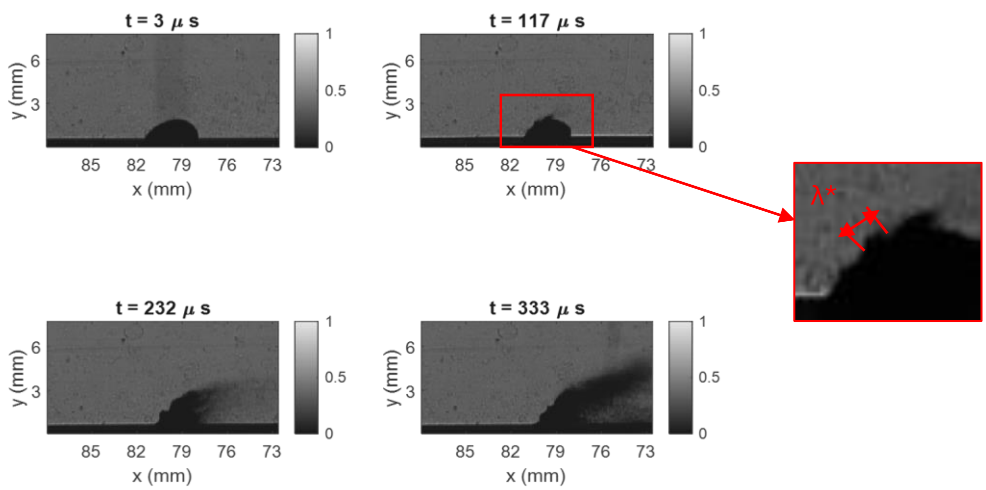

Figure 23: Time Progression of a non-hydrophobic droplet with a diameter of 2.7 mm and unit Reynolds number of 5.0×10^{6} 1/m with the total breakup zoomed for instability visualization

The above figure illustrates the breakup of a liquid droplet for condition 2. It should be noted that the contact angle on each side for the non-hydrophobic surface is different by a non-negligible amount. This is a phenomenon known as Contact Angle Hysteresis (CAH), which has been documented by [32]. This occurs when the relative velocity between the droplet and the ground is nonzero. This means that the shock tube moves slightly upstream when the diaphragm actuates, as well before the shockwave passes, the droplet is symmetrical. It is also remarkable that the hydrophobic droplet does not experience the contact angle hysteresis. This can be explained due to the nature of a hydrophobic surface with low surface free energy. This means that the water molecules are more attracted to other water molecules than to the molecules of the surface. In other words, the droplets cohesion forces are higher than the adhesion forces. As a result, as the shock tube moves slightly forward when the fast acting valve opens, the droplet slides over the moving surface, unaffected by the phenomenon. Notably, the instability wavelengths appear, and are also 6 pixels in length.

Nevertheless, the leading edge contact angle should be the one for consideration, as the upstream instabilities are attributed to the Rayleigh Taylor Piercing (RTP) that occurs from the impulse like increase of pressure interacting with the liquid droplet [33]. Therefore, the leading edge contact angle will be the main parameter to look at for the analysis of surface wettability on the aero breakup of a wall-laden droplet. One notable takeaway from figure 11 is that the Rayleigh Taylor Piercing occurs almost 100 microseconds earlier for the non-hydrophobic case compared to the hydrophobic case. Additionally, the hydrophobic wettability resulted in the droplet breakup on both the top and bottom portion of the droplet on the leeward side. However, for the non-hydrophobic case, the droplet primarily breaks up from the top surface of the droplet. This is likely due to Shear-Induced Entrainment (SIE), in which a region of recirculation is formed on the leeward side of the droplet, causing Kelvin-Helmholtz instabilities to occur. These instabilities lead to the leeward side deformation. It should be noted that due to the velocity difference between the top surface of the droplet and the bottom of the droplet, Kelvin-Helmholtz instabilities can also form at the top surface of the droplet, which can interact with the Rayleigh-Taylor instabilities as well. The point of analysis for this case will be considering the Rayleigh-Taylor instabilities, since the flattening of the upstream surface seen by these experiments is typically associated with the Rayleigh-Taylor Piercing. Nevertheless, Since the hydrophobic droplet has a larger expansion towards the leeward side, the region in which the Kelvin-Helmholtz instabilities form is much larger, allowing for breakup in multiple locations towards the downstream side of the droplet [34].

Comparatively, the effect of the freestream Reynolds number on the breakup of the droplet is also of importance. Therefore, the time evolution of a hydrophobic droplet with a contact surface angle of 135°, a diameter of 2.68 mm at a freestream Reynolds number of 8.4×10^{6} is analyzed.

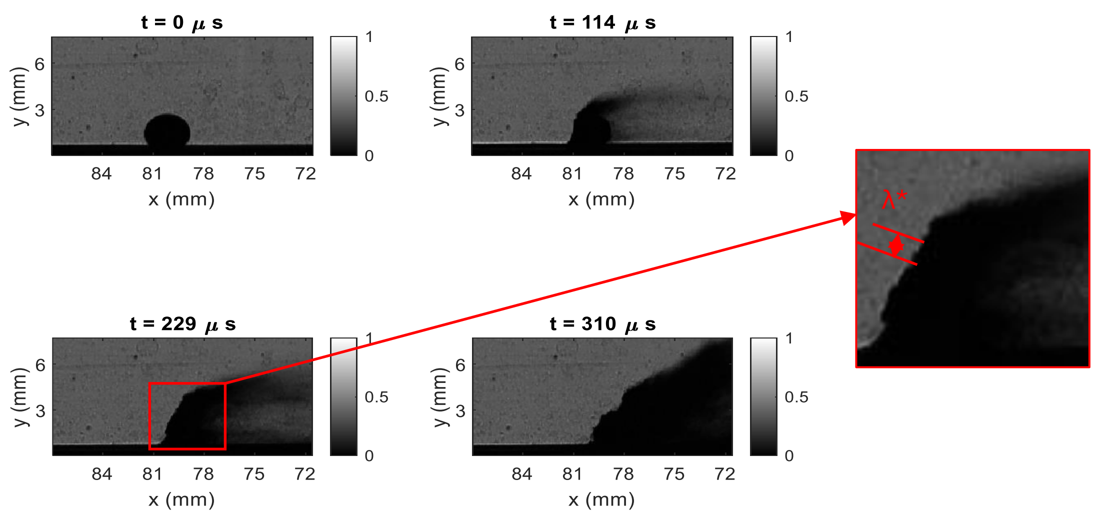

Figure 24: Time Progression of a hydrophobic droplet with a diameter of 2.68 mm and unit Reynolds number of 8.4×10^{6} 1/m with the total breakup zoomed for instability visualization

The time history for condition 5 is shown above. The initial breakup is very similar to that of figure 23. One of the main differences between the two time histories is that the higher unit Reynolds number case rapidly deforms by Shear Induced Entrainment as seen by 100 microseconds and 200 microseconds later. Additionally, the instabilities on the upstream surface of the droplet seem to decrease in wavelength, as they are just under 5 pixels in wavelength. Similarly, the breakup of a non-hydrophobic droplet is to be analyzed at a unit Reynolds number of 8.4×10^6 1/m, attachment angle of 70°, and a diameter of 2.7 mm are visualized below.

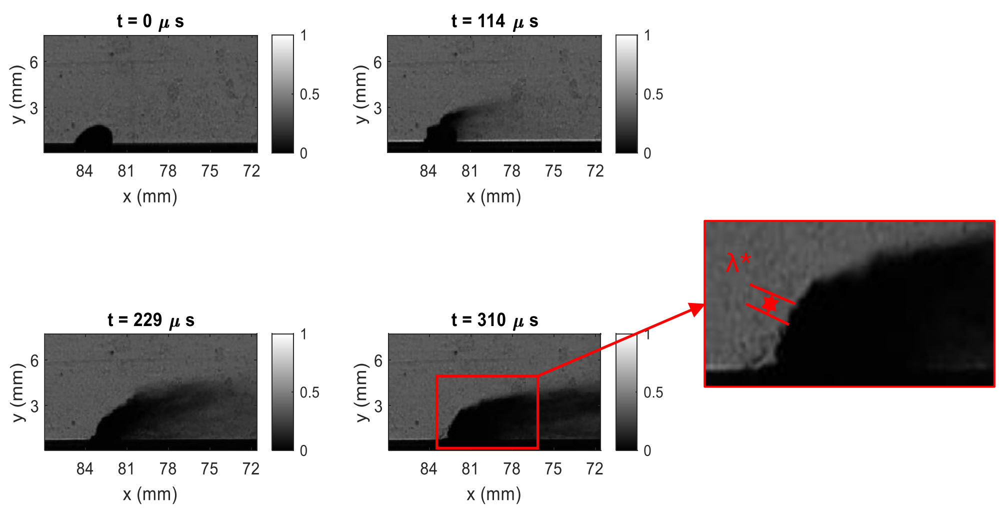

Figure 25: Time Progression of a non-hydrophobic droplet with a diameter of 2.7 mm and unit Reynolds number of 8.4×10^6 1/m with the total breakup zoomed for instability visualization

The time history of the droplet breakup for condition 6 is illustrated in the figure above. The instabilities on the upstream side of the droplet take longer to fully develop on the non-hydrophobic droplet for this case. One other nontrivial observation is that at 200 microseconds, at the leading edge contact point between the droplet and the surface, a small liquid film can be seen to form (it resembles a bump by the leading edge contact angle on the surface at 300 microseconds). This phenomenon has been documented by [19] for contact angles less than 90°, and is reflected in the experiments conducted. Additionally, the shear induced entrainment for this case also seems to increase, as the deformation on the leeward side of the droplet is also much greater than the non-hydrophobic case for a freestream Reynolds number of $5.0 * 10^6$ 1/m. Similar to condition 5, the droplet in condition 6 has smaller instability wavelengths of about 5 pixels. It should also be noted that although it makes sense for the higher unit Reynolds number to increase the deformation caused by the shear induced entrainment (since dynamic pressure in the freestream is nearly double than in figure 22), it has been previously studied that an increased weber number can also result in the increased breakup caused by shear induced entrainment. Therefore, in order to compare the effects caused by freestream Reynolds number and how the droplet breaks up, the weber number must remain constant. This can be accomplished by altering the diameter of the droplet. This can result in a uniform weber number while studying the effects of unit Reynolds number. Therefore, to keep the weber number constant with the condition in Figure 24, the freestream Reynolds number used in Figures 22 and 23 will be employed, while the diameter of the droplet is increased to 4.36 mm. As a result, the Weber number of the conditions in Figure 24 and 25, along with the new condition is about 3300. Thus, the droplet breakup structure was analyzed at a freestream Reynolds number of 4.9×10^6 1/m and a diameter of 4.36 mm with a contacting angle of 135°.

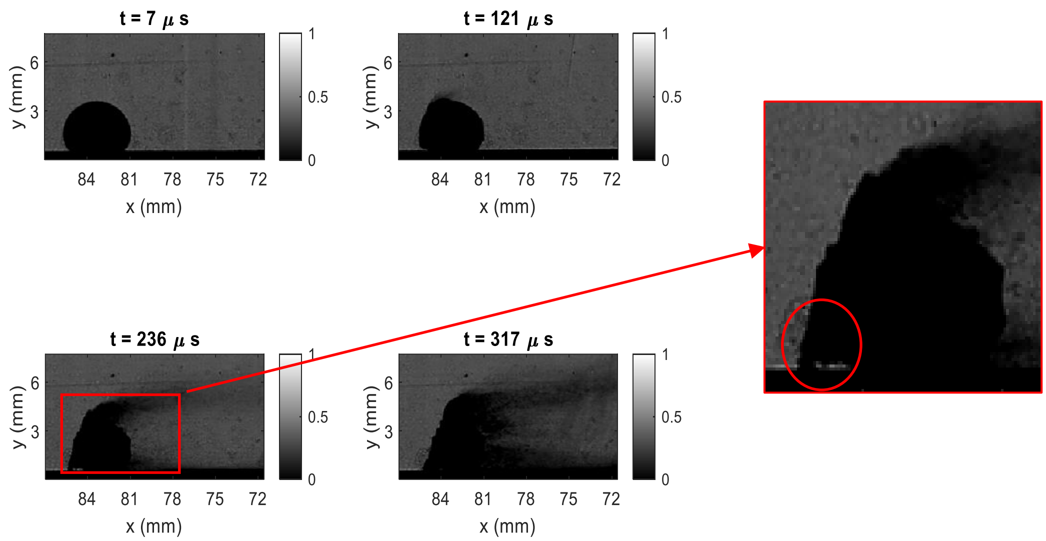

Figure 26: Time Progression of a hydrophobic droplet with a diameter of 4.36 mm and unit Reynolds number of 4.9×10^{6} 1/m with the total breakup zoomed for notable flow structures

The aerobreakup for condition 13 is shown above. The comparison between the condition in Figure 26 and Figure 25 show that the aero breakup caused by the shear induced entrainment is greater in the case of a larger unit Reynolds number than the case of a smaller unit Reynolds number. This result is intuitive, but remarkable, as it illustrates breakup caused by shear induced entrainment is not solely a function of Weber number. The wavelength of the instabilities for this condition is found to be 5 pixels, which is less than condition 1 at the same freestream unit Reynolds number, but is equivalent to condition 5, which is at the equivalent Weber number. Additionally, a novel structure that has not been reported in previous literature was observed on the upstream surface of the droplet near the surface. In the circled region of figure 19, there seems to be a large vortex that formed. The vortex can be visualized by seeing trapped gas between the leftmost contact point and the mean mass of the droplet, which is much lighter in these cases. This vortex near the windward attachment point was not observed for the droplet of 2.7 mm. This means that the recirculation region is an effect of diameter, rather than Weber number. Further research can be completed investigating the formation of this complex flow structure.

Nevertheless, the droplet at 84° and a 4.42 mm with a unit Reynolds number of 4.9×10^{6} 1/m is to be analyzed.

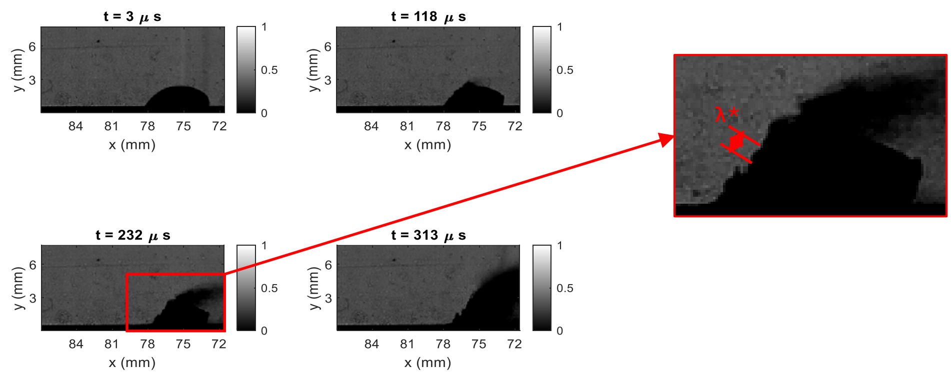

Figure 27: Time Progression of a non-hydrophobic droplet with a diameter of 4.42 mm and unit Reynolds number of 4.9×10^{6} 1/m with the total breakup zoomed for notable flow structures

Condition 14 is analyzed for the time history of the droplet. Figure 27 depicts the breakup of a non-hydrophobic droplet for the condition mentioned previously. The instability wavelength is found to be about 5 pixels. This verifies the findings from condition 13, in which the consistent Weber number yields consistent instability wavelengths, despite different unit Reynolds number and diameter. It is evident that similar to the hydrophobic case, even though the weber number is constant with conditions 6 and 13, the breakup caused by shear induced entrainment is reduced in the lower unit Reynolds number case. Since this is the case for the non-hydrophobic and hydrophobic cases, it can be concluded that the breakup of a liquid droplet caused by shear induced entrainment is not only a function of weber number, but also of unit Reynolds number.

4.3: Further Analysis

To analyze the deformation of the droplet, the breakup of the droplets was nondimensionalized in each spatial dimension along with nondimensional time. To nondimensionalize the characteristics of the droplet, the methods used by [35] are employed to give a nondimensionalized time the following relationship:

$$t^* = t * \frac{U_2}{d} \sqrt{\rho_2/\rho_d} \tag{10}$$

Where t is the time when the incident normal shock wave hits the leading edge of the wall laden droplet, and the asterisk denotes nondimensionalization. It should be noted that the nondimensional time depends on diameter, so any trends involving a changing diameter should consider this and look at how nondimensional time and dimensional time affect the behavior. In addition, the width (W), height (H), and leading edge displacement (S), are all variables of interest, as knowing how a droplet deforms as a function of time is very important to understanding the breakup characteristics of a liquid droplet. The image below illustrates how each variable is defined:

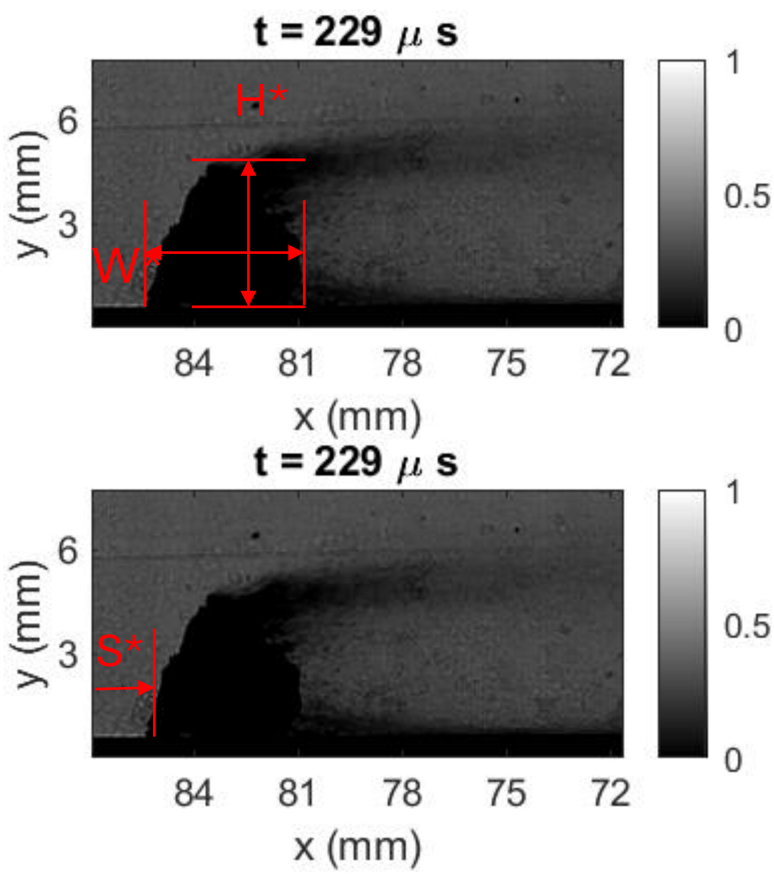

Figure 28: Definitions of Deformation Variables a) W and H b) S

The above figure illustrates the definitions of a droplet's width, height, and leading edge displacement for condition 13. The width is the most nonintuitive definition, as the shear induced entrainment deformation results in a much larger width than what is actually recorded. Previous research defines W as the main droplet width deformation, meaning no "peaking" structures such as the top edge deformation. Height on the other hand is defined by the maximum height of the deforming droplet, which increases quickly. Finally, the leading-edge displacement is defined as the distance travelled by the leading edge contact angle. However, the film by the leading edge seen in the non-hydrophobic case previously should be ignored. Thus, the nondimensionalization of these variables can be defined. The historical definition of each nondimensional variable can be seen by the relations below:

$$W^* = 1 + \frac{W - W_0}{d} \tag{11}$$

Where W* is the nondimensional width as a function of time, W is the width as a function of time, and W_0 is the initial width, or diameter, of the droplet. Similarly, the nondimensional height of the droplet as a function of time is seen below:

$$H^* = 1 + 2\frac{(H - H_0)}{d} \tag{12}$$

Where H* is the nondimensional height as a function of time, H is the height as a function of time, and H_0 is the initial height of the droplet. It is multiplied by a scaling factor of two. This is because in the historical data of [23], the base condition was a contact angle of 90°. In order to compare the results found in this experiment with previous research, the scaling factor will be utilized for this experiment as well. Finally, the leading edge displacement is normalized and found to be:

$$S^* = \frac{S - S_0}{d} \tag{13}$$

Where S* is the nondimensional leading edge displacement as a function of time, S is the leading edge position as a function of time, S_0 is the initial leading edge position at the initial condition. Additionally, previously literature found that the wall effect causes a liquid film to appear on the upstream side of the droplet, and this was ignored when tracking the leading edge deformation. It should be considered that after nondimensionalization, the initial points of W* and H* should be 1, and S* should be zero. This physically makes sense as the width and height should have value, while the displacement should be zero since the droplet hasn't moved.

Utilizing the canny method, along with verifying the pixel intensity as a function of time, the nondimensional width as a function of time was tracked for each condition, and each test was averaged for the corresponding condition. Then a trend for nondimensional width and nondimensional time, along with a trend for nondimensional width and dimensional time were found for the lowest unit Reynolds number.

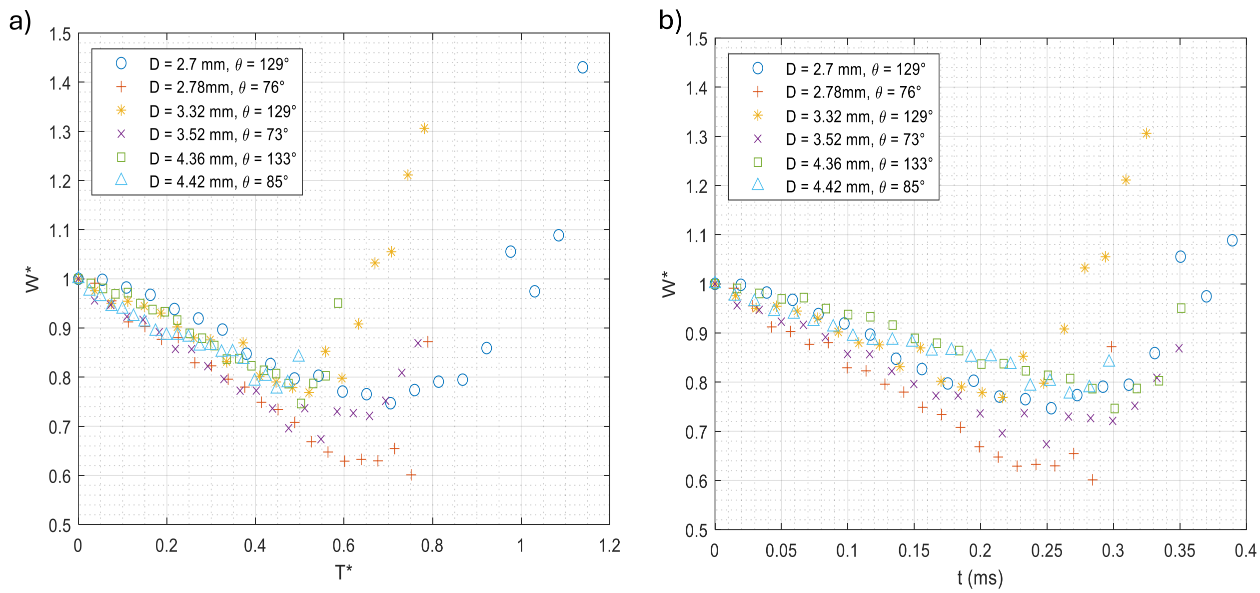

Figure 29: Time evolution of nondimensional Width for a liquid droplet at a unit Reynolds number of $5.0{\times}10^6$ 1/m for a) nondimensional time and b) time after the shockwave passes the droplet in milliseconds

The figure depicts how the nondimensional width of a droplet changes as a function of time for a droplet hit by a shock wave for conditions 1, 2, 7, 8, 13, and 14 respectively. It is found from that the width of the droplet decreases with contact angle. It is also found that the nondimensional width begins to rapidly increase in a faster nondimensional time as the diameter gets bigger. However, this is just a result of how nondimensional time is calculated and why analysis should be carefully considered before proceeding. The main relationship found in figure 29b is that the non-hydrophobic surface decreases in width at a faster rate than the hydrophobic surface for the small and medium droplets, while the large droplets have a small change between the hydrophobic and non-hydrophobic surfaces. In addition, the medium sized droplet on the hydrophobic surface seems to increase its width rapidly faster than any other condition. This could potentially be reaching an optimized case for increasing the width in the shortest amount of time, but more research must be conducted to make any conclusions about this one observation.

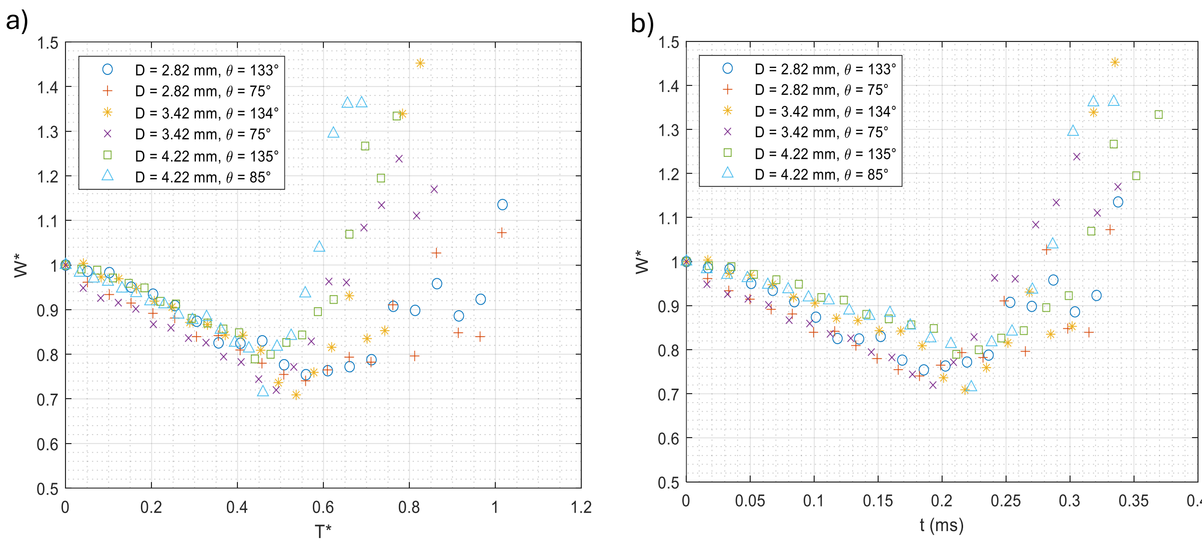

Figure 30: Time evolution of nondimensional Width for a liquid droplet at a unit Reynolds number of 6.5×10^{6} 1/m for a) nondimensional time and b) time after the shockwave passes the droplet in milliseconds

The figure depicts how the nondimensional width of a droplet changes as a function of time for a droplet hit by a shock wave for conditions 3, 4, 9, 10, 15, and 16respectively. Similar to the previous conditions, the non-hydrophobic surfaces for the small and medium diameters decrease in width at a faster rate than the hydrophobic surfaces. However, the large droplet does not seem to differ based off the hydrophobic surfaces. Additionally, the condition in figure 30b that peaked early is not seen to occur at a higher unit Reynolds number. It can also be concluded that as the diameter increases for figure 30b, the width of the droplet decreases at a slower rate. The nondimensional width of the droplet as a function of time can also be visualized for the conditions of a unit Reynolds number equal to 8.5×10^6 1/m, which can be seen in the figure below:

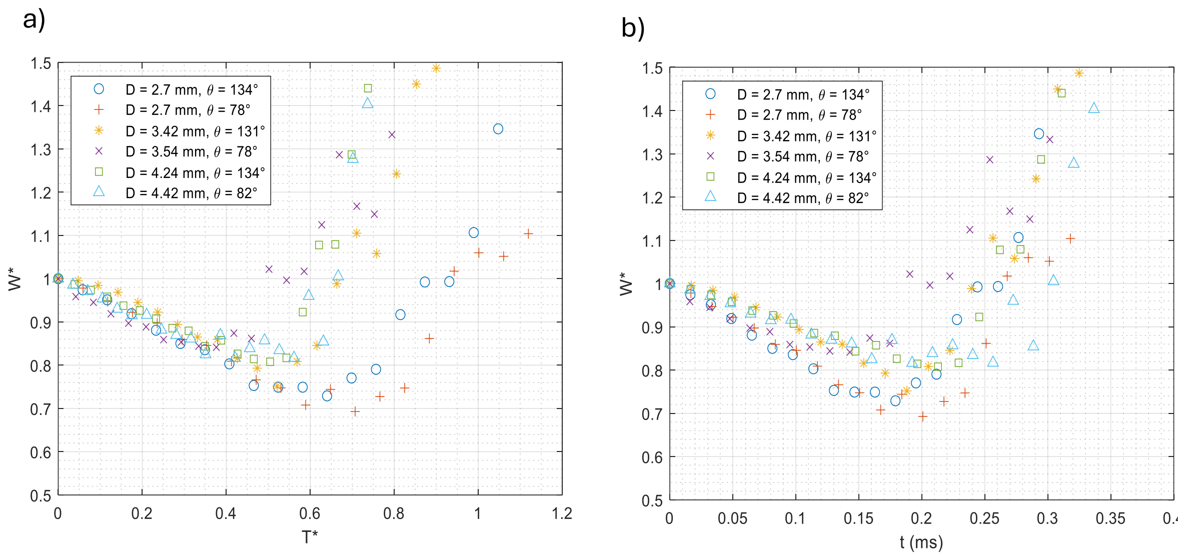

Figure 31: Time evolution of nondimensional Width for a liquid droplet at a unit Reynolds number of 8.5×10^6 1/m for a) nondimensional time and b) time after the shockwave passes the droplet in milliseconds

The figure depicts how the nondimensional width of a droplet changes as a function of time for a droplet hit by a shock wave for conditions 5, 6, 11, 12, 15, and 16 respectively. Contrary to the previous conditions, Figure 31b illustrates that for the medium sized droplet, the non-hydrophobic surface results in a faster decrease in the width than the hydrophobic surface, but for the large sized droplet, the non-hydrophobic surface also decreases in width slightly faster than the hydrophobic surface. Additionally, the small sized droplet does not seem to have a large relationship with the attachment angle and the initial decrease in width. The overall trend of the smaller diameter decreasing in width still seems to hold, although the medium sized droplet on the hydrophobic surface is seen to decrease at the slowest rate. Nevertheless, the results analyzed in this case are all for different weber numbers, so to properly compare the results, weber number should be held constant to ensure a proper relationship between another parameter. Figure 32 illustrates the nondimensional width relationship with the time after the shock passes the droplet at a constant Weber number of 3345.

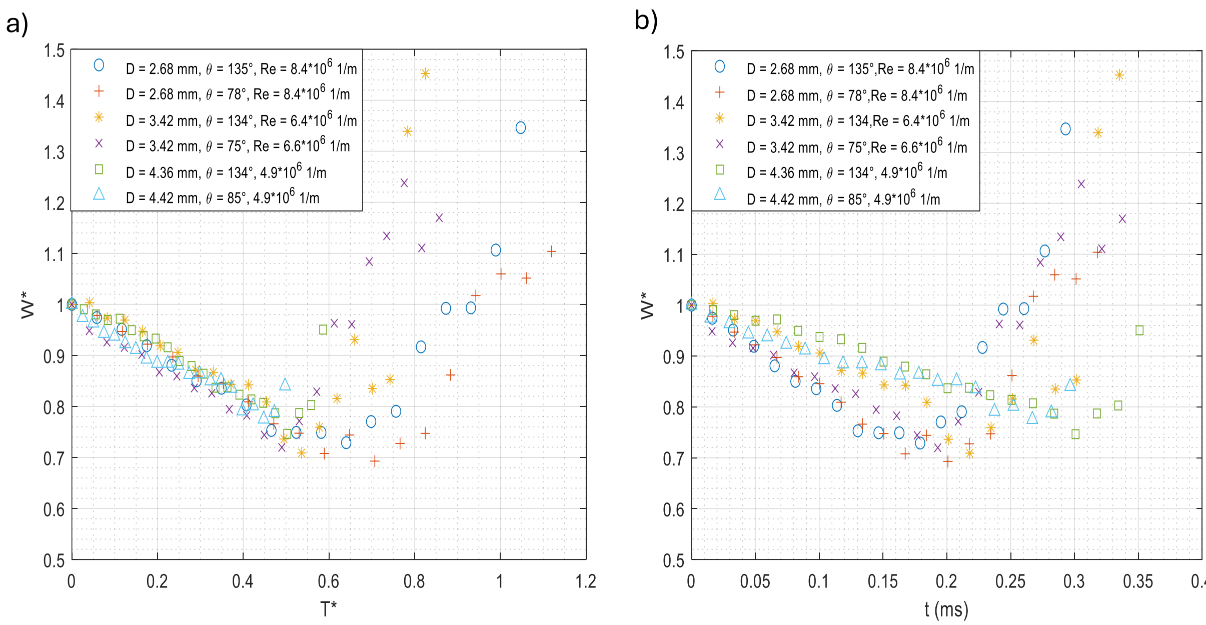

Figure 32: Time evolution of nondimensional Width for a liquid droplet at We = 3345 for a) nondimensional time and b) time after the shockwave passes the droplet in milliseconds

The trend is shown for conditions 5, 6, 9, 10, 13, and 14 respectively. It can be elucidated that the trends discussed earlier hold true for a constant weber number and are best seen for the same weber number as well. Specifically, the non-hydrophobic surface reflects a faster decrease in width initially compared to the hydrophobic surface, except for the small diameter droplet. Another conclusion that is confirmed is that the decreasing droplet size results in a faster decrease in width as well, which holds true for all cases reflected in figure 32b. It is also seen that the total breakup for every droplet occurs roughly around 0.2 ms. This should be investigated for a wider range of diameters and unit Reynolds number to see the consistent trends. Finally, the point in which the droplet completely breaks up and starts increasing in width happens sooner for smaller diameters with higher freestream Reynolds numbers. This is intuitive as a higher dynamic pressure over a droplet with less inertia should result in the complete breakup of the droplet before a droplet with more inertia in a smaller dynamic pressure. Overall, the trends for nondimensional width with time progression for different sized droplets in different freestream Reynolds numbers with different surface wettabilities have been characterized. It is also important to investigate how these parameters investigate nondimensional height. Nondimensional height is a very important variable to study, as a large nondimensional height would mean a more successful atomization of the droplet, as the dispersion is tightly tied to the atomization of the droplet. Therefore, the nondimensional height is observed for different diameters and contact angles with the surface at a unit Reynolds number of 5.0×10^6 1/m. Figure 33 illustrates the relationship between these parameters.

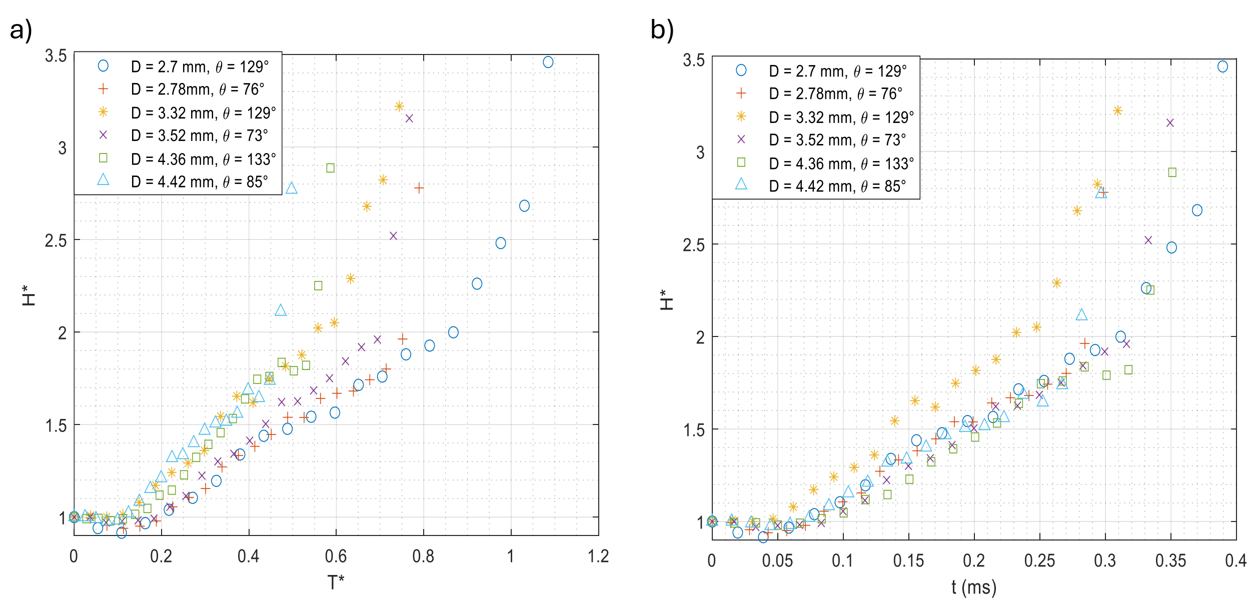

Figure 33: Time evolution of nondimensional Height for a liquid droplet at a unit Reynolds number of 5.0×10^6 1/m for a) nondimensional time and b) time after the shockwave passes the droplet in milliseconds

The nondimensional height as a function of time for conditions 1, 2, 7, 8, 13, and 14 respectively for the breakup of a liquid droplet in a shock tube is reflected in the figure above. One initial observation is that there is not a clear relationship between the change in height of the droplet as a function of time between different diameters. Additionally, before the absolute breakup at just after 250 microseconds and after the initial breakup at about 50 microseconds, the relationship between the change in height and the time after the initial shockwave passes the droplet is seen to be very linearly. On the other hand, there is not a consistent trend that can be observed with how the diameter affects the nondimensional height. Similarly, the attachment angle does not have a consistent trend with the height of the droplet. Nevertheless, the height of the droplet at a unit Reynolds number of $6.5*10^6$ 1/m can also be observed.

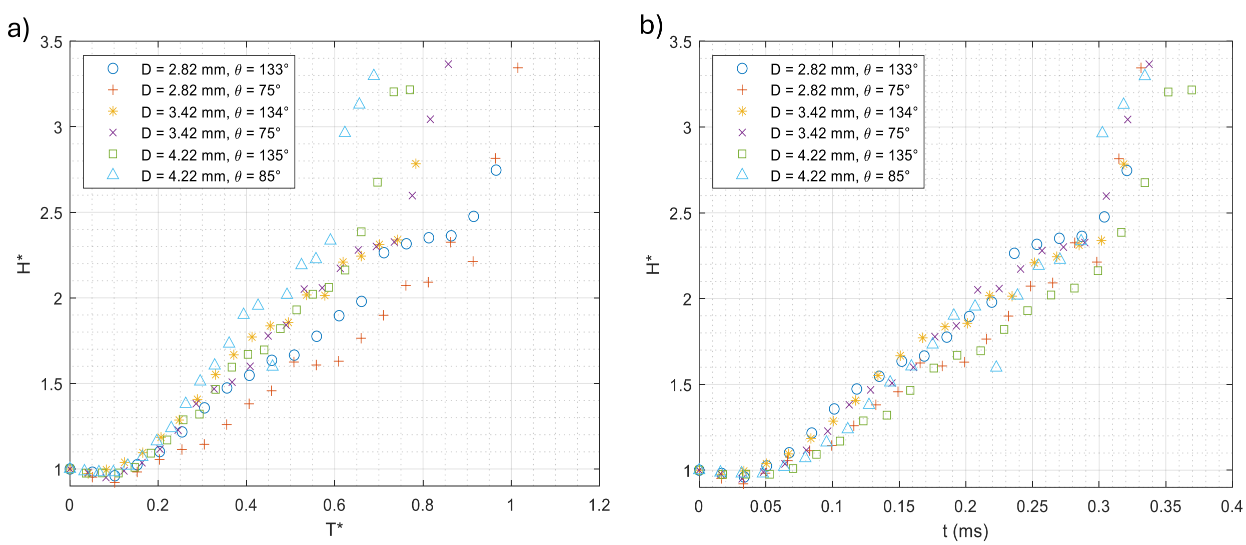

Figure 34: Time evolution of nondimensional Height for a liquid droplet at a unit Reynolds number of 6.5×10^6 1/m for a) nondimensional time and b) time after the shockwave passes the droplet in milliseconds

The nondimensional height as a function of time for conditions 3, 4, 9, 10, 15, and 16 respectively for the breakup of a liquid droplet in a shock tube is reflected in the figure above. The current condition illustrates the same conclusion as the previous condition, in which the trend is roughly linear after the initial breakup of the droplet. However, the slope of the linear portion can be seen to increase by a factor of about 1.76, as the average slope goes from about $3.3*10^5$ 1/s to about $5.8*10^5$ 1/s. It is likely that the rate of change of this slope is caused by the change of density, which increased by a factor of about 1.3. To further analyze this trend, the height as a function of time is found for the unit Reynolds number of $8.5*10^6$ 1/m.

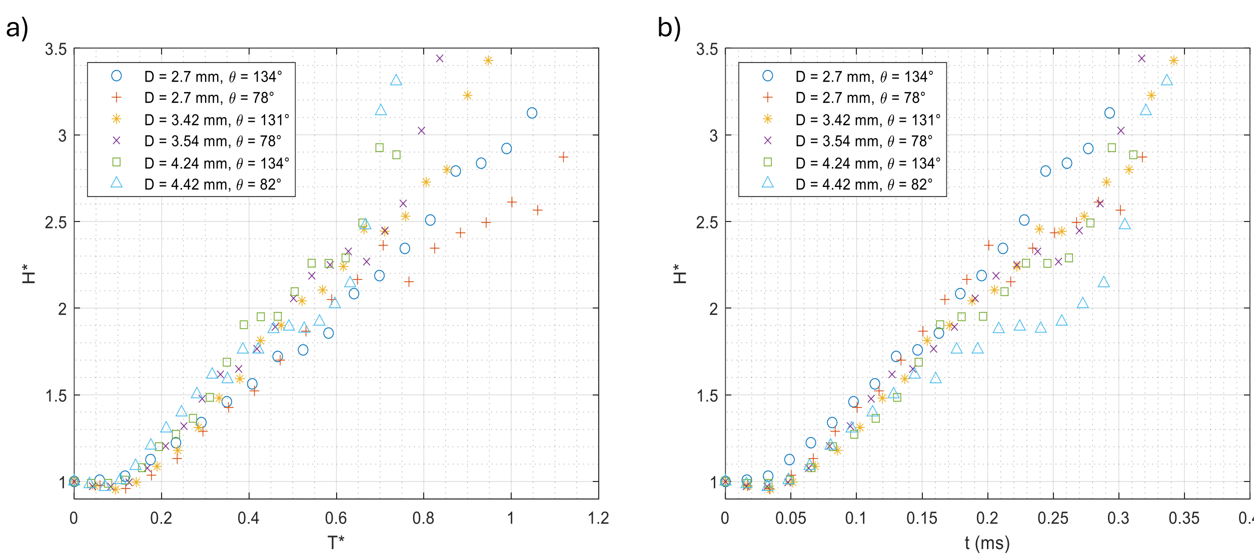

Figure 35: Time evolution of nondimensional Height for a liquid droplet at a unit Reynolds number of 8.5×10^6 1/m for a) nondimensional time and b) time after the shockwave passes the droplet in milliseconds

Conditions 5, 6, 11, 12, 17, and 18 are considered for their change in nondimensional height as a function of time for the breakup of a water droplet in a shock tube. It is found that the slope of the linear portion of Figure 35b increases as the freestream Reynolds number increases. The new slope value is on the order 7.5×10^5 1/s, which increased the slope from Figure 34b by a factor of 1.29, and an increase of slope from Figure 33b by a factor of 2.27. Meanwhile, the density at a unit Reynolds number of 8.5×10^6 1/m increases by a factor of 1.31 for 34b, and a factor of 1.7 for 33b. Therefore, it is possible the freestream unit Reynolds number is directly tied to this change in slope observed for each condition. To ensure this is the case, the tests with the same weber number should be compared. If the cases with lower unit Reynolds numbers have a less steep slope, then the freestream Reynolds number is found to also impact the height deformation of the droplet.

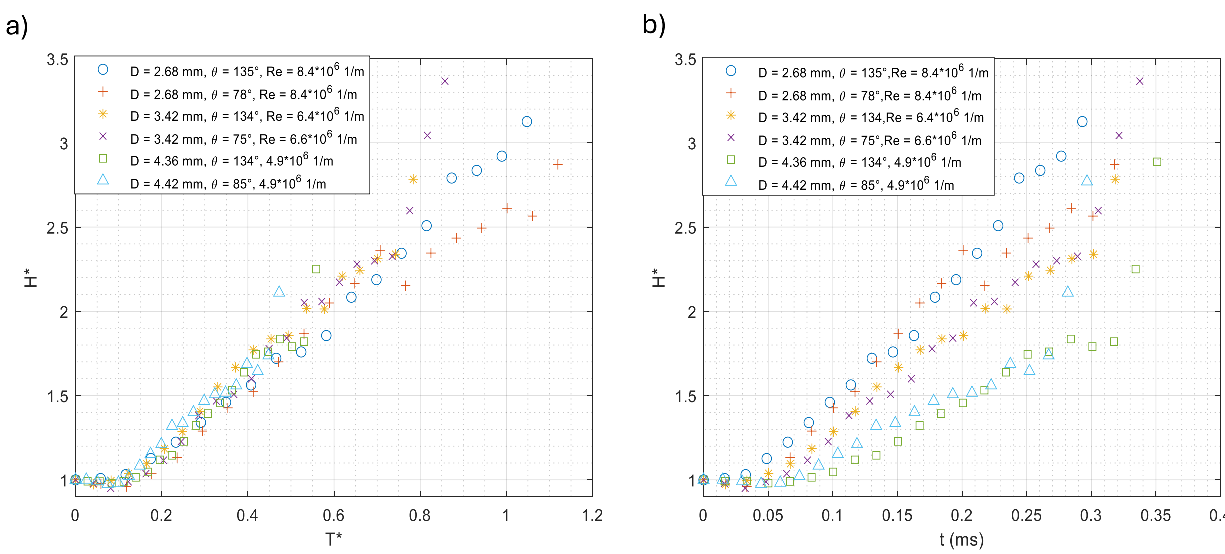

Figure 36: Time evolution of nondimensional Height for a liquid droplet at We = 3345 for a) nondimensional time and b) time after the shockwave passes the droplet in milliseconds

To keep weber number constant, conditions 5, 6, 9, 10, 13, and 14 are all considered. The trends seen previously are also found for this condition. That is, as the freestream unit Reynolds number increases with a decrease in diameter, the rate at which the height changes also increases. Most importantly, this trend is seen for a constant Weber number. Therefore, further investigations could be implemented to find a relationship with how the change in height evolves with different unit Reynolds numbers. Finally, it is important to know how the droplet is being displaced through time. The displacement as a function of time can be used to find the acceleration of the droplet, which is used to not only find force but to find the theoretical instabilities that are propagated onto the droplet caused by Rayleigh-Taylor Piercing. Therefore, the displacement as a function of time is found for the smallest unit Reynolds number condition, and can be seen in the figure below:

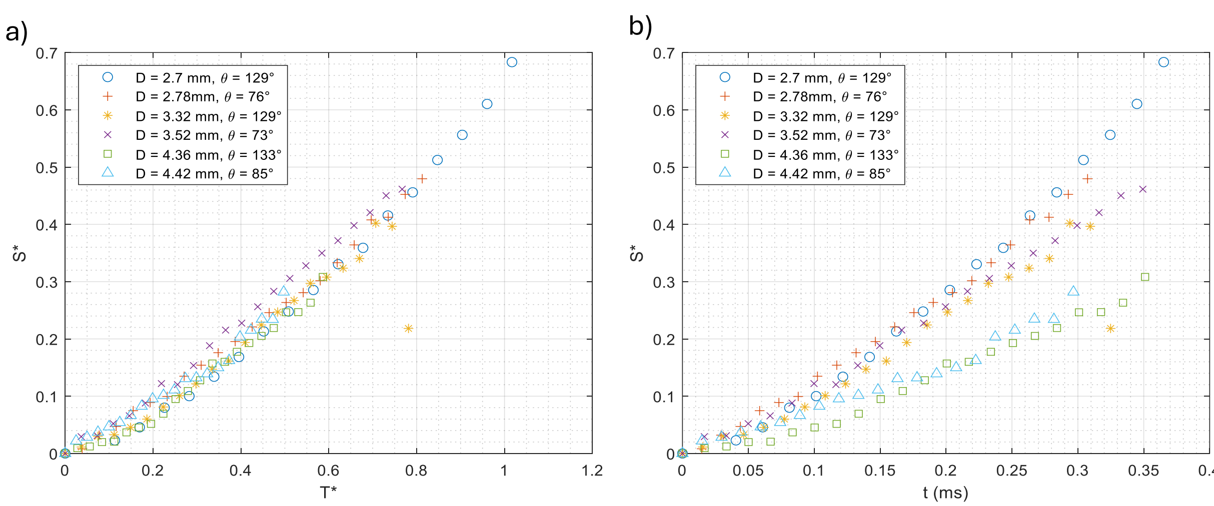

Figure 37: Time evolution of nondimensional leading edge displacement for a liquid droplet at a unit Reynolds number of 5.0×10^{6} 1/m for a) nondimensional time and b) time after the shockwave passes the droplet in milliseconds

The normalized leading edge displacement as a function of time for conditions 1, 2, 7, 8, 13, and 14 respectively for the breakup of a liquid droplet in a shock tube is reflected in the figure above. It is observed that smaller diameters are displaced at a much faster rate according to figure 37b. This is intuitive, as the smaller diameters have less mass, and therefore more acceleration in the same flow condition. This trend is also seen in figures 38b, and 39b.

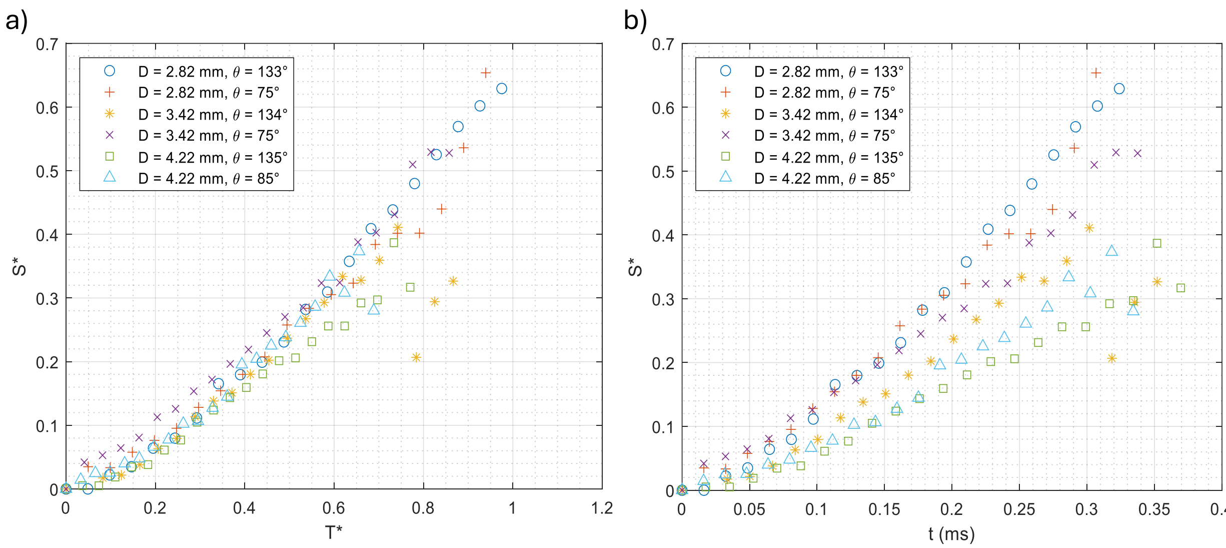

Figure 38: Time evolution of nondimensional leading edge displacement for a liquid droplet at a unit Reynolds number of 6.5×10^{6} 1/m for a) nondimensional time and b) time after the shockwave passes the droplet in milliseconds

Conditions 3, 4, 9, 10, 15, and 16 and their effect on leading edge displacement for the aerobreakup of a liquid droplet in a shock tube are reflected in the image above.

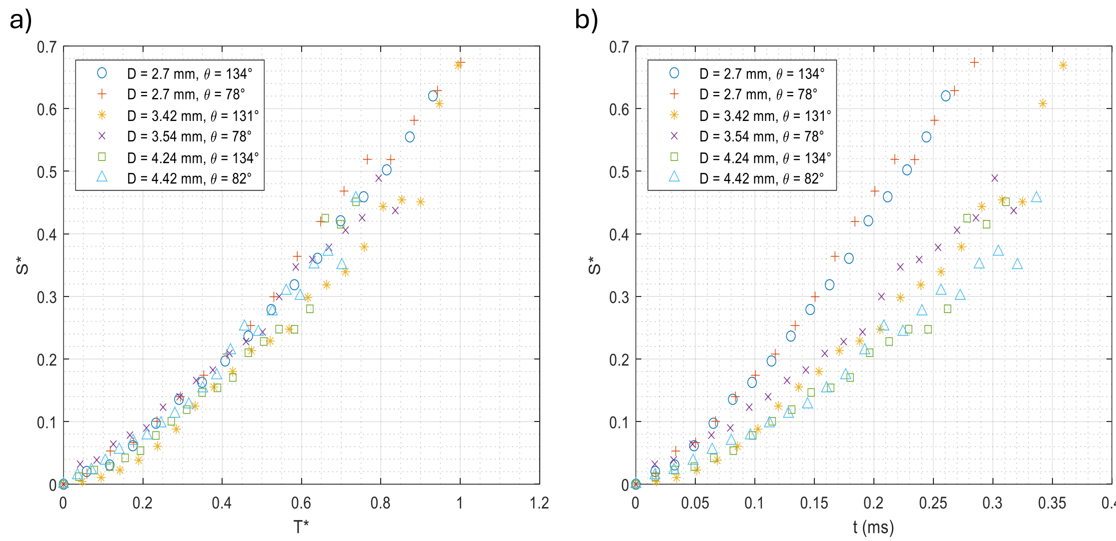

Figure 39: Time evolution of nondimensional leading edge displacement for a liquid droplet at a unit Reynolds number of 8.5×10^6 1/m for a) nondimensional time and b) time after the shockwave passes the droplet in milliseconds

Conditions 5, 6, 11, 12, 17, and 18 and their effect on leading edge displacement for the aerobreakup of a liquid droplet in a shock tube are reflected in the image above. Figures 38 and 39 illustrate the similar trend seen in Figure 37, in which the smaller diameters have a larger leading edge displacement as a function of time. Finally, in order to ensure the trends seen above are accurate and not caused by changing Weber number, the different conditions for a constant Weber number are also observed in the figure below:

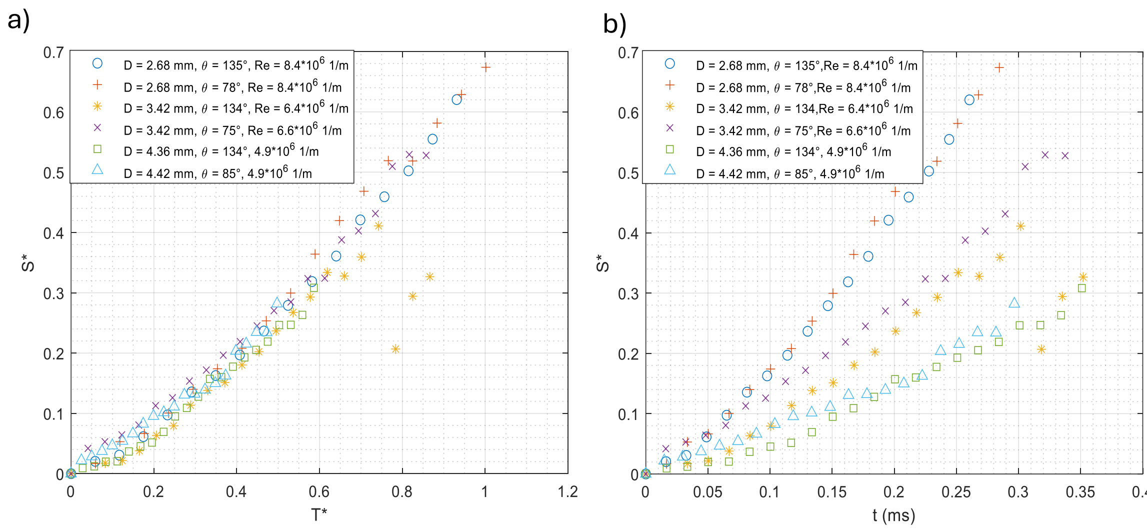

Figure 40: Time evolution of nondimensional leading edge displacement for a liquid droplet at We = 3345 for a) nondimensional time and b) time after the shockwave passes the droplet in milliseconds

Conditions 5, 6, 9, 10, 13, and 14 are all compared to find the freestream unit Reynolds number and diameter as a function of time. The Weber number is kept constant in order to ensure the trend is not due to the change in Weber number. It is thus verified that the role of diameter and freestream unit Reynolds number has the expected result. It is also notable that the non-hydrophobic droplets become displaced faster than the hydrophobic droplets. This also makes sense for the same reason, as they have the same diameter, but the non-hydrophobic droplets have less volume, and therefore less mass. Thus, this behavior is expected. Nevertheless, dimensionless acceleration can be obtained from the previous findings by fitting a quadratic polynomial with a y-intercept of zero to the displacement data. This is because the nondimensional acceleration is related to the second derivative of the nondimensional displacement. As a result, after taking the quadratic curve fit for the displacement over time figures, the nondimensional acceleration can be found by doubling the leading coefficient. After the nondimensional acceleration is found, it can be converted to actual acceleration with the following relation:

$$a = a^* \frac{U_2^2}{d} \frac{\rho_l}{\rho_2} \tag{14}$$

Where a is the acceleration, a* is the nondimensional acceleration, and ρ_l is the density of the water. Once a is calculated, the coefficient of drag can be found by considering the methods used by [36]:

$$C_D = \frac{Ma}{qS} = \frac{\left(\frac{2}{3}\pi R^3(1-\cos(\theta))\right)\rho_l * a}{\frac{1}{2}\rho_2 U_2^2 * S} \tag{15}$$

Where M is the mass of the droplet, q is the local dynamic pressure, R is the radius of curvature of the droplet, and S is the reference area the flow passes over. S is found by using MATLAB to find the area under the droplet using the Canny method edge detection. It should be noted that this reference area is not the traditional perpendicular planform area that is implemented, as the limitations of shadowgraphs resulting in a 2D geometry make it impossible to estimate that area for a wall-laden droplet. Therefore, this area will solely be used as an estimation, and the results will be compared to the coefficient of drag calculations for a spherical water droplet found by Wang et Al. [22]. The coefficient of drag was calculated for different sized droplets at different diameters and unit Reynolds numbers. The relationship between the coefficient and drag and diameter of the liquid droplet is reflected below:

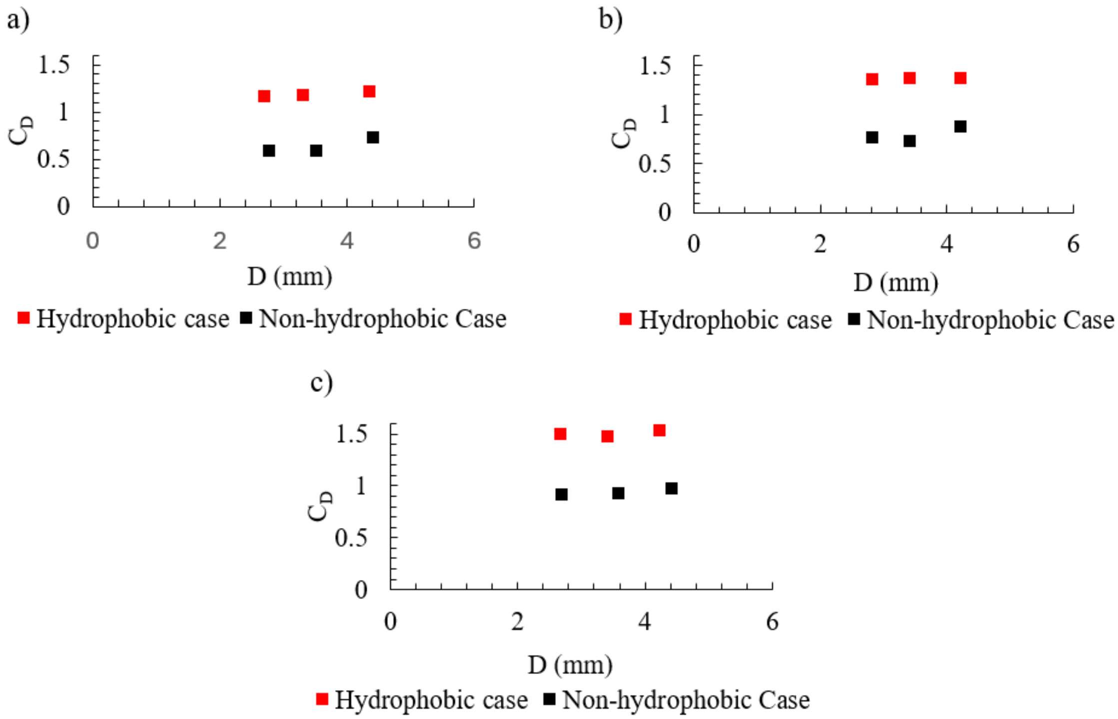

Figure 41: Coefficient of Drag for the Aerobreakup of a Liquid Droplet at Different Diameters for a) a unit Reynolds number of 5.0×10^{6} 1/m, b) a unit Reynolds number of 6.5×10^{6} 1/m, c) a unit Reynolds number of 8.5×10^{6} 1/m

The conditions reflected are conditions 1, 2, 7, 8, 13, and 14 for figure 41a, conditions 3,4, 9, 10, 15, 16 are shown in figure 41b, and conditions 5, 6, 11, 12, 17, and 18 are shown in figure 41c. The main observation from this relationship illustrates that the coefficient of drag does not significantly change as the diameter of the droplet changes. This is fairly consistent with expected results. It should be noted that the value of the coefficient of drag is significantly high compared to the expected value for a sphere which is about 0.5. However, the aerobreakup of a fully spherical liquid droplet has historically been found to range between 0.8 and 1.4 for transonic freestream mach numbers [22]. Therefore, the values found by the method proposed above is on the same order of magnitude, with the error possibly being attributed to the different area being considered. Another observation is that the coefficient of drag is significantly lower for non hydrophobic droplets compared to the hydrophobic cases. The coefficient of drag for a hemisphere is naturally 80% the original value of the coefficient of drag for a sphere. However, the drag over the hemispherical droplet for the aerobreakup of a liquid droplet is about 60% of the original value for a sphere. This is much lower compared to the rigid case, and should be noted for future experiments. The relationship between the coefficient of drag and the unit Reynolds number can also be visualized below:

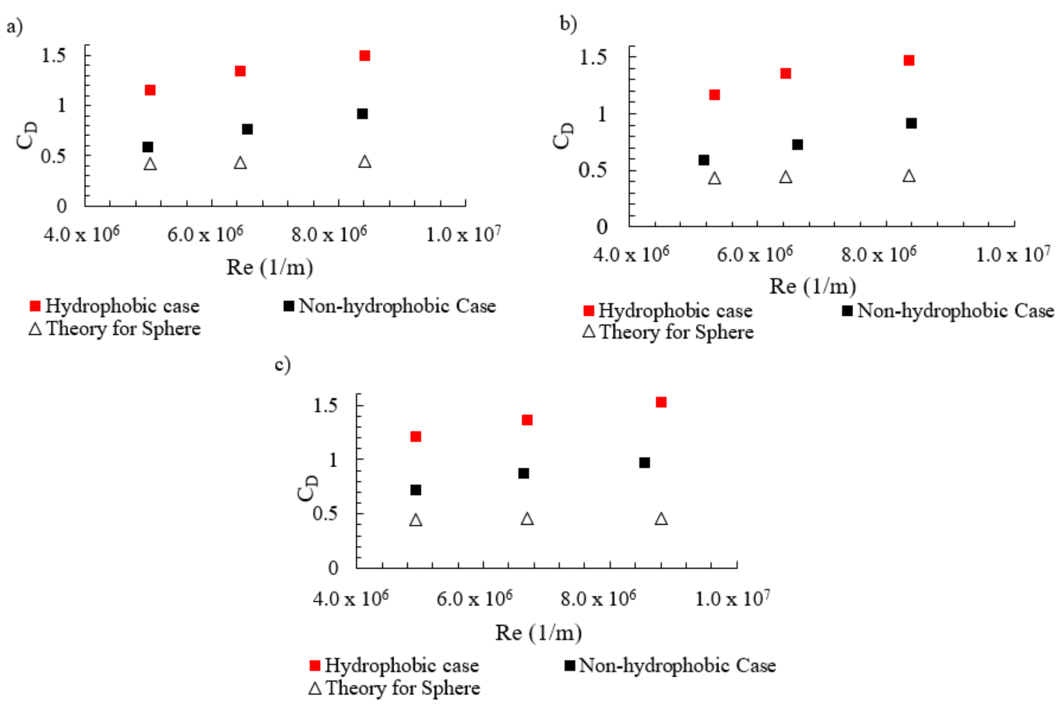

Figure 42: Relationship between coefficient of drag and unit Reynolds number for a) a diameter of 2.75 mm, b) a diameter of 3.45 mm, and c) a diameter of 4.31 mm

The conditions reflected are conditions 1, 2, 3, 4, 5, and 6 for figure 42a, conditions 7, 8, 9, 10, 11, and 12 are shown in figure 42b, and conditions 13, 14, 15, 16, 17, and 18 are shown in figure 42c. The trend has a clear relationship in which the coefficient of drag for a hemisphere increases as the unit Reynolds number increases. The coefficient of drag is found to increase by about 15% for each case. The rate at which the coefficient of drag increases also seems to decrease as unit Reynolds number is increased. Therefore, a higher density should result in an increased displacement of a water droplet. The trend of attachment angle is also reflected in Figure 42 as it was previously, in which the coefficient of drag for a hemisphere is about 60% of the original value. It is also notable that the theoretical coefficient of drag for a rigid sphere also increases with unit Reynolds number, as the dimensionless Reynolds number is on the order of 10^4 for these conditions, in which the coefficient of drag should increase with Reynolds number. However, due to the flattening of the liquid droplet, the experimental coefficient of drag is much higher than the case of a theoretical rigid sphere. This has been historically recorded by Wang et Al., as they found values for the coefficient of drag between 0.8 and 1.4 [22].

Finally, a notable point of analysis on the breakup of these droplets is the instability wavelengths that occur on the upstream side of the droplet. The instabilities were visualized previously, and a more in depth analysis is to be conducted. First, these wavelengths are considered to be produced by Rayleigh-Taylor Piercing. [25] can be used to find the theoretical wavelength values of the instabilities. The theoretical wavelength values is dependent on the acceleration found from the droplet, and therefore the attachment angle will have a significant effect on the instability wavelengths, which is found by [24]. That is, the following relationship is employed to begin the theoretical calculation of the instability wavelengths.

$$\omega_{RT}^* = -{k_{RT}^*}^2 * \frac{c}{Re} \pm \sqrt{k_{RT}^* \frac{a^*}{c^2} - {k_{RT}^*}^3 \frac{1}{c^2 We} + {k_{RT}^*}^4 * \frac{1}{Re}} \qquad (16)$$

Where ω_{RT}^{*} is the nondimensionalized temporal growth rate of the Rayleigh-Taylor perturbations and ${k_{RT}^{*}}^{2}$ is the nondimensionalized wave number. c is defined by:

$$c = \frac{\mu_l}{\mu_2}\sqrt{\frac{\rho_l}{\rho_2}} \tag{17}$$

The relationship between the wave number and temporal growth rate can then be visualized for different wave numbers, and is seen below:

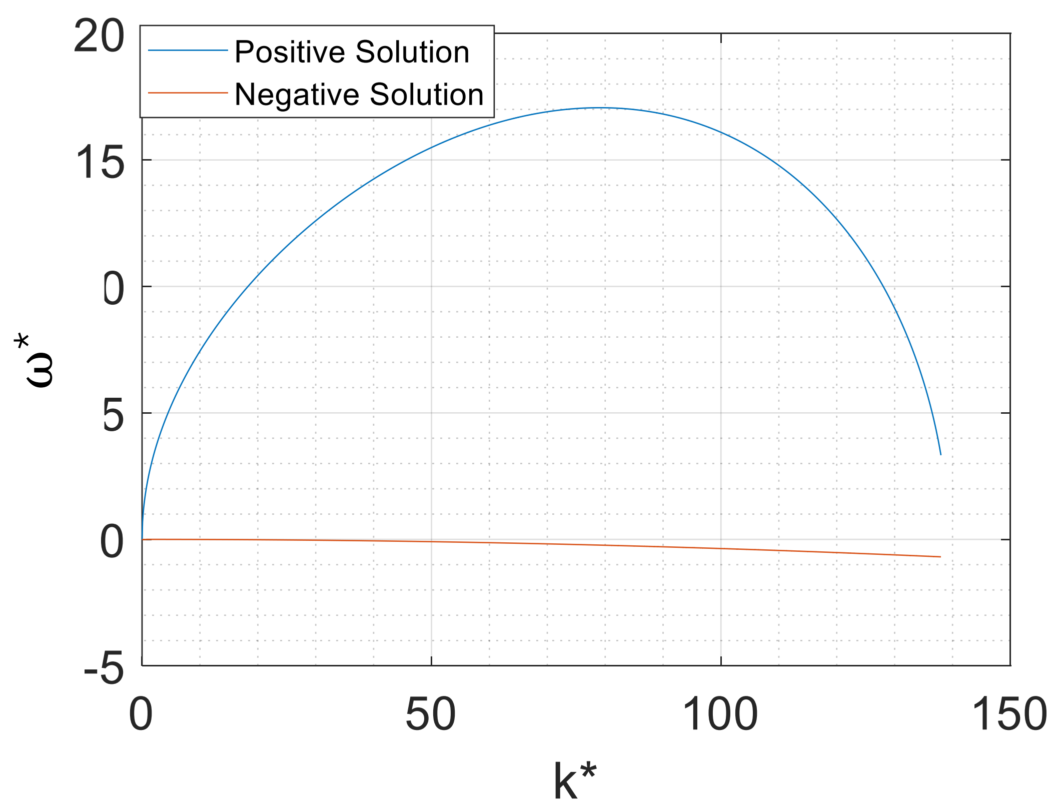

Figure 43: Dependance of Nondimensional Temporal Growth Rate with Nondimensional Wave Number

The relationship reflected in the figure above was found for condition 5. The positive solution in the figure corresponds to the positive discriminant in equation 17, while the negative solution corresponds to the negative discriminant in equation 17. It can be concluded from figure 43 that the nondimensional temporal growth rate for the Rayleigh-Taylor instabilities reaches some maximum value based off the nondimensional acceleration, Reynolds number, and Weber number. The nondimensional wave number at which this maximum value occurs can be utilized to calculate the normalized wavelengths of the instabilities by:

$$\lambda_{RT}^{*} = \frac{2\pi}{k_{RT\,max}^{*}} \tag{18}$$

Finally, the actual wavelengths of the instabilities can be found by multiplying the initial diameter size of the droplet. The relationship between the diameter of the droplet and the wavelength of the instabilities caused by Rayleigh Taylor Piercing is reflected in the figure below:

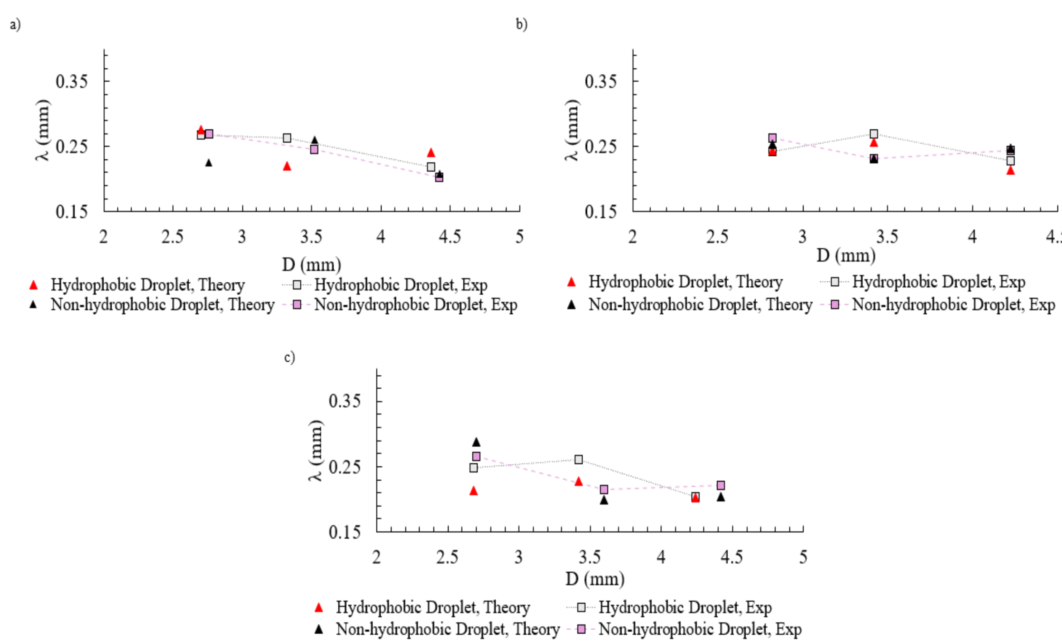

Figure 44: Relationship between Rayleigh Taylor Instability Wavelengths (mm) and Diameter (mm) for a) a unit Reynolds number of 5.0×10^6 1/m, b) a unit Reynolds number of 6.5×10^6 1/m, c) a unit Reynolds number of 8.5×10^6 1/m

The conditions reflected are conditions 1, 2, 7, 8, 13, and 14 for figure 44a, conditions 3,4, 9, 10, 15, 16 are shown in figure 44b, and conditions 5, 6, 11, 12, 17, and 18 are shown in figure 44c. The general trend visualized is that the Rayleigh-Taylor instabilities estimated with both visualization and theoretical calculation illustrate a general decreasing trend. There are some notable differences between the hydrophobic case and the non-hydrophobic case. For all unit Reynolds numbers, the hydrophobic case is concave down in both theoretical calculations and experimental visualizations, while the non-hydrophobic case is concave up for both theory and experiment. A concave down relationship means that the instability reaches a maximum value at some diameter before decreasing, while a concave up relationship results in a minimum instability value for some diameter and then instability wavelengths increase as diameter increases. This means that there is some angle at which the Rayleigh-Taylor instabilities likely have no concavity, and the relationship is solely linear. This would be useful to discover exactly how a droplet breaks up in a certain condition. It may also be useful to visualize the relationship between the instability wavelengths of the droplet and the unit Reynolds number. The relationship is shown below:

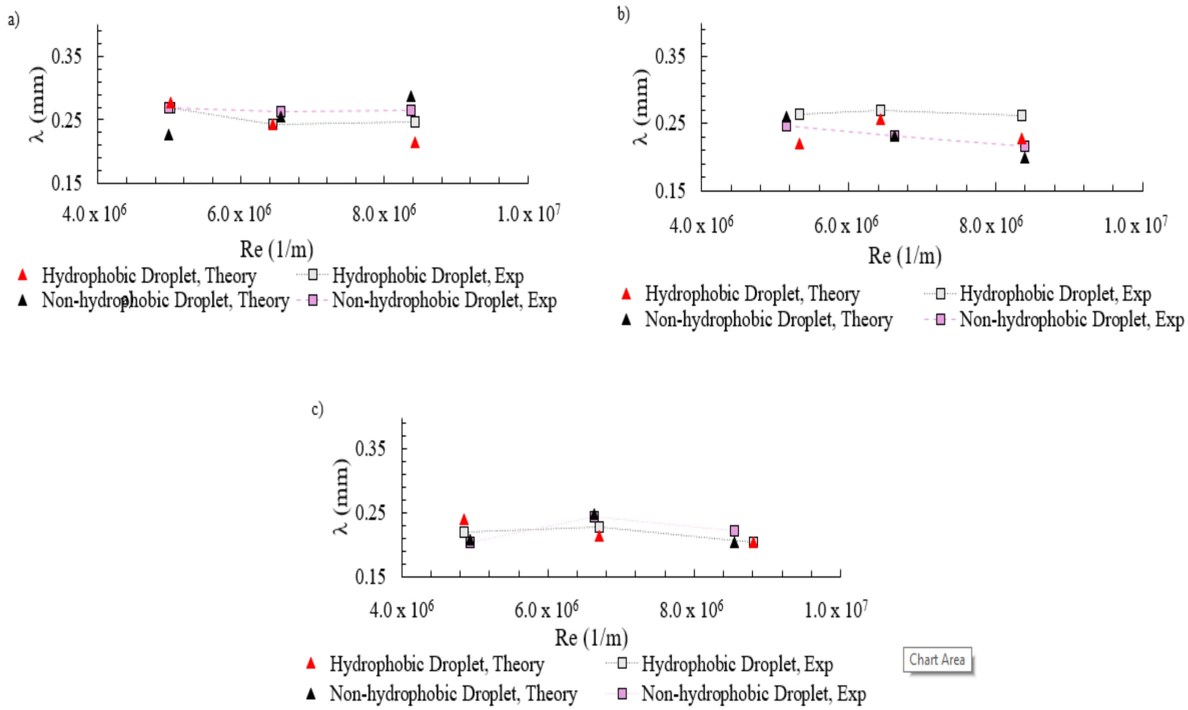

Figure 45: Relationship between Rayleigh Taylor Instability Wavelengths (mm) and unit Reynolds number (1/m) for a) a diameter of 2.75 mm, b) a diameter of 3.45 mm, c) a diameter of 4.31 mm

The conditions reflected are conditions 1, 2, 3, 4, 5, and 6 for figure 45a, conditions 7, 8, 9, 10, 11, and 12 are shown in figure 45b, and conditions 13, 14, 15, 16, 17, and 18 are shown in figure 45c. It is found that the unit Reynolds number has a small impact on the experimental values for the instability wavelengths. Additionally, the smallest diameter case (D = 2.75 mm), shows a near constant relationship for the wavelength and unit Reynolds number for the non hydrophobic case experimentally. The relationships for larger diameters transition into a concave down relationship, meaning the instability wavelengths reach a maximum value before decreasing. The non-hydrophobic and hydrophobic case show very similar results experimentally for increasing unit Reynolds numbers. For future testing, more data points at these different locations should be investigated to find a more refined relationship between these instabilities and the different test parameters.

Conclusion

Different parameters and their effect on the aerobreakup of a wall attached droplet on a shock tube wall were investigated to determine how the droplet breaks up in various conditions. Specifically, the diameter of the liquid droplet, unit Reynolds number of the freestream gas, and attachment angle of the droplet-surface interface, were all varied to characterize their effect on the nature of the breakup of the droplet. General flow structures, deformation characteristics as a function of time, drag characterization, and instability analysis were all examined in order to characterize the effects of the changing parameters. PCB pressure measurements were also recorded to characterize the freestream conditions of the flow. The analysis of the PCB pressure measurements in region 2 illustrated an insignificant impact produced by the presence of the droplet, allowing for the freestream conditions to be repeatable for different sized droplets. Shadowgraph photography was implemented to visualize the breakup. New flow structures such as a vortex on the droplet-surface interface was found on the upstream side of the droplet. This structure has never been documented and was only observed for a diameter of 4.31 mm. The deformation of each droplet was also tracked. Observing the normalized width as a function of time found that the total breakup of the droplet occurred at 0.2 ms no matter what parameter was used. It was also found that the non-hydrophobic droplet decreased in width initially at a faster rate than the hydrophobic droplet. A linear trend was observed between the normalized height as a function of time for each condition tested. A novel finding is the increase seen in the rate that the normalized height increased was proportional to the increase in unit Reynolds number, even at a constant Weber number of 3345. This illustrates the dependance of density on the nondimensional height for the breakup of a droplet. The leading edge displacement was also found for the droplet. In cases of higher unit Reynolds numbers and lower diameters, the droplet was displaced at a higher rate than the other conditions.

The coefficient of drag for each case was also found. The acceleration of each droplet was found by using quadratic regression on the normalized displacement as a function of time. The coefficient of drag was then found from simple dynamics, which found different values for each parameter. Although the coefficient of drag had a relatively constant value for different diameter droplets, increasing the unit Reynolds number increased the coefficient of drag by about 15%. On the other hand, the drag for the non-hydrophobic case was about 60% of the value of the hydrophobic case. This was a new finding, as rigid bodies of the same geometry yield about 80% of the original value of a spherical case.

Finally, the wavelengths of the instabilities that were visualized were analyzed by measuring their wavelengths. The theoretical values that depend on the experimental acceleration, weber number, and Reynolds number were compared to the experimental values. There was a large discrepancy in the general trends for the hydrophobic case and non-hydrophobic case as diameter changed. The hydrophobic case had a maximum wavelength for the conditions tested, while the non-hydrophobic case had a minimum wavelength for the different diameters. However, the trends between wavelengths and unit Reynolds number were fairly similar between the hydrophobic and non-hydrophobic cases. The theory was also within reason of the experimental values.

For future testing, many new research areas were opened up as a result for some of the findings. Since several comparisons with attachment angle effect have been made on the breakup regime of water droplets, other parameters can be tested instead. For example, by using different test gases in the shock tube or using different liquid compositions for the droplets, different Weber numbers can be achieved while keeping the nondimensional Reynolds number constant, which is not possible with using the same liquid and gas. Additionally, larger Weber numbers greater than 6000 can be examined to further investigate the vortex like behavior at the attachment point would be useful to further analyze the phenomenon. Finally, only three different variations of the same inertial parameter were conducted in this experiment. Specifically, the density or diameter of the droplet only changed by a factor of about 1.7. Therefore, testing over a much larger range could see the trends expanded such that a total understanding of how a droplet breaks up in different conditions is obtained. More specifically, the general trends concluded for the instability wavelengths and coefficients of drag could be further expanded on. In addition, laser induced florescence could be used to visualize the breakup of the droplet in tandem with high speed photography at different points of view. This would be to overcome the limitations of the two-dimensional plane visualization that occurs with shadowgraph photography. As a result, the coefficient of drag and instability wavelengths could be better refined. Overall, there are many opportunities to further the understanding of shock induced aerobreakup on a wall laden droplet, but this paper serves as a foundation for the understanding of several important trends in application.

References

[1] Jihuan He, Approximate analytical solution of Blasius' equation, Communications in Nonlinear Science and Numerical Simulation, Volume 3, Issue 4,1998,Pages 260-263,ISSN 1007-5704, https://doi.org/10.1016/S1007-5704(98)90046-6.

[2] Mirels, H., "Laminar Boundary Layer behind Shock Advancing into Stationary Fluid," Mar 01 1955.

[3] Stratford, B. S., and Beavers, G. S., "The Calculation of the Compressible Turbulent Boundary Layer in an Arbitrary Pressure Gradient—A Correlation of Certain Previous Methods," *Reports and Memoranda*, No. 3207, Ministry of Aviation Aeronautical Research Council, London, 1961.

[4] M. Lagha, J. Kim, J. D. Eldredge, X. Zhong; A numerical study of compressible turbulent boundary layers. *Physics of Fluids* 1 January 2011; 23 (1): 015106. https://doi.org/10.1063/1.3541841

[5] Herring, H. J., and Mellor, G. L., "A Method of Calculating Compressible Turbulent Boundary Layers," *NASA Contractor Report*, No. CR-1144, Princeton Univ., Princeton, NJ, prepared for Lewis Research Center, NASA, Washington, DC, Sept. 1968.

[6] Steven Schroeder, Sheikh Salauddin, Anthony Morales, Miguel Moran, Rachel Hytovick, Egan Rigney, Kareem Ahmed, Deformation and aerobreakup of RP-2 droplets from hypersonic shock waves, Proceedings of the Combustion Institute, Volume 40, Issues 1–4, 2024, ISSN 1540-7489, https://doi.org/10.1016/j.proci.2024.105338.

[7] T. G. Theofanous, V. V. Mitkin, C. L. Ng, C-H. Chang, X. Deng, S. Sushchikh; The physics of aerobreakup. II. Viscous liquids. *Physics of Fluids* 1 February 2012; 24 (2): 022104. https://doi.org/10.1063/1.3680867

[8] L.-P. Hsiang, G.M. Faeth, Drop deformation and breakup due to shock wave and steady disturbances, International Journal of Multiphase Flow, Volume 21, Issue 4, 1995, Pages 545-560, ISSN 0301-9322, https://doi.org/10.1016/0301-9322(94)00095-2.

[9] Yaozhi Zhou, Zun Cai, Qinglian Li, Chenyang Li, Mingbo Sun, Peibo Li, Hongbo Wang, Review of atomization mechanism and spray characteristics of a liquid jet in supersonic crossflow, Chinese Journal of Aeronautics, Volume 36, Issue 8, 2023, Pages 1-23, ISSN 1000-9361, https://doi.org/10.1016/j.cja.2023.03.010.

[10] Mahmood, T. and Ling, Y., "Aerodynamic breakup of submillimeter drops in high-speed flows", Art. no. Q17.004, 2021.

[11] Z. Xu, T. Wang, and Z. Che, "Droplet breakup in airflow with strong shear effect," *Journal of Fluid Mechanics*, vol. 941, p. A54, 2022. doi:10.1017/jfm.2022.326

[12] YoungJun Kim, James C. Hermanson; Breakup and vaporization of droplets under locally supersonic conditions. *Physics of Fluids* 1 July 2012; 24 (7): 076102. https://doi.org/10.1063/1.4733459

[13] Troitskaya, Y., Kandaurov, A., Zotova, A., Korsukova, E. V., and Sergeev, D., "Statistical Characteristics of Droplets Formed Due to the 'Bag Breakup' Fragmentation Event at the Interface Between Water and High-Speed Air Flow," *Journal of Physical Oceanography*, Vol. 53, No. 10, 2023, pp. 2331–2352. https://doi.org/10.1175/JPO-D-23-0037.1.

[14] Culick, F. & Rogers, T.. (1985). The Response of Normal Shocks in Diffusers. AIAA Journal. 21. 10.2514/3.8257.

[15] Yaozhi ZHOU, Zun CAI, Qinglian LI, Chenyang LI, Mingbo SUN, Peibo LI, Hongbo WANG, Review of atomization mechanism and spray characteristics of a liquid jet in supersonic crossflow, Chinese Journal of Aeronautics, Volume 36, Issue 8, 2023, Pages 1-23, ISSN 1000-9361, https://doi.org/10.1016/j.cja.2023.03.010.

[16] Lefebvre, A.H. & McDonell, V.G. 2017 Atomization and Sprays. CRC

[17] Alpher, R. A., and White, D. R., "Flow in Shock Tubes with Area Change at the Diaphragm Section," Journal of Fluid Mechanics, Vol. 3, No. 05, 1958, p. 457. https://doi.org/10.1017/S0022112058000124

[18] "Sutherland's Law." Retrieved 19 July 2024. https://doc.comsol.com/5.5/doc/com.comsol.help.cfd/cfd_ug_fluidflow_high_mach.08.27 . html

[19] Guildenbecher DR, López-Rivera C, Sojka PE. Secondary atomization. Exp Fluids. 2009;46(3):371–402. doi: 10.1007/s00348-008-0593-2. [DOI] [Google Scholar]

[20]: Pilch, M. & Erdman, C.A. 1987 Use of breakup time data and velocity history data to predict the maximum size of stable fragments for acceleration-induced breakup of a liquid drop. Intl J. Multiphase Flow 13 (6), 741–757.

[21] Theofanous TG, Li GJ. On the physics of aerobreakup. Phys Fluids. 2008;20(5):052103. doi: 10.1063/1.2907989

[22] Wang, Z., Hopfes, T., Giglmaier, M., and Adams, N. A., "Effect of Mach Number on Droplet Aerobreakup in Shear Stripping Regime," *Experiments in Fluids*, Vol. 61, No. 9, 2020, p. 193. doi:10.1007/s00348-020-03026-1

[23] Ranger AA, Nicholls JA. Aerodynamic shattering of liquid drops. AIAA J. 1969;7(2):285–290. doi: 10.2514/3.5087

[24] Guo, J., Kang, P., Mu, K., Li, J., and Si, T., "On Shock-Induced Aerobreakup of a Wall-Attached Droplet," *Journal of Fluid Mechanics*, Vol. 971, 2023, p. A31. doi:10.1017/jfm.2023.612.

[25] Joseph, D.D., Belanger, J. & Beavers, G.S. 1999 Breakup of a liquid drop suddenly exposed to a high-speed airstream. Intl J. Multiphase Flow 25 (6–7), 1263– 1303.

[26] Schmucker, J.A., Osterhaut, J.C. & White, E.B. 2012 Speckle technique for dynamic drop profile measurement on rough surfaces. Exp. Fluids 52 (1), 123–136.

[27] Hooshanginejad, A. & Lee, S. 2017 Droplet depinning in a wake. Phys. Rev. Fluids 2 (3), 031601.

[28] Bicak, A. “Influence of Freestream Reynolds Number on Unsteady Reflected Normal Shockwave Boundary Layer Interactions in Shock Tube Experiments”. *Masters Thesis*, Department of Aerospace and Mechanical Engineering, University of Oklahoma, Norman, OK, 2024.

[29] R. Gupta, V. Vaikuntanathan, D. Sivakumar, Superhydrophobic qualities of an aluminum surface coated with hydrophobic solution NeverWet, Colloids and Surfaces A:

Physicochemical and Engineering Aspects, Volume 500, 2016, Pages 45-53, ISSN 0927-7757, https://doi.org/10.1016/j.colsurfa.2016.04.017.

[30] Sadullah, M.S., Xu, Y., Arunachalam, S. *et al.* Predicting droplet detachment force: Young-Dupré Model Fails, Young-Laplace Model Prevails. *Commun Phys* **7**, 89 (2024). https://doi.org/10.1038/s42005-024-01582-0

[31] J. Canny, "A Computational Approach to Edge Detection," in *IEEE Transactions on Pattern Analysis and Machine Intelligence*, vol. PAMI-8, no. 6, pp. 679-698, Nov. 1986, doi: 10.1109/TPAMI.1986.4767851

[32] Hans-Jürgen Butt, Jie Liu, Kaloian Koynov, Benedikt Straub, Chirag Hinduja, Ilia Roismann, Rüdiger Berger, Xiaomei Li, Doris Vollmer, Werner Steffen, Michael Kappl,Contact angle hysteresis,Current Opinion in Colloid & Interface Science,Volume 59,2022,101574,ISSN, 1359-0294, https://doi.org/10.1016/j.cocis.2022.101574.

[33] B.D. Fishburn, Boundary layer stripping of liquid drops fragmented by Taylor instability, Acta Astronautica, Volume 1, Issues 9–10, 1974, Pages 1267-1284, ISSN 0094-5765, https://doi.org/10.1016/0094-5765(74)90051-4.

[34] Senoner, J.-M. "On Drop Aerobreakup in the Shear Induced Entrainment Regime." 2024. ffhal04589474.

[35] Meng, J.C. & Colonius, T. 2018 Numerical simulation of the aerobreakup of a water droplet. J. Fluid Mech. 835, 1108–1135.

[36] Bailey AB, Haitt J. Sphere drag coefficients for a broad range of Mach and Reynolds numbers. AIAA J. 1972;10(11):1436–1440. doi: 10.2514/3.50387.

Appendix

APPENDIX A

$$\frac{A_4}{A_1} = \frac{1}{M_{3a}}\left(\frac{(2+(\gamma_4-1)M_{3a}^2}{2+\gamma_4-1}\right)^{\left(\frac{\gamma_4+1}{2*(\gamma_4-1)}\right)}$$

$$T_2 = T_1\left(1+\frac{2\gamma_1}{\gamma_1+1}(M_s^2-1)\right)\frac{(2+(\gamma_1-1)M_s^2)}{(\gamma_1+1)M_s^2}$$

$$g = \left(\frac{(2+(\gamma_4-1)M_{3a}^2}{2+\gamma_4-1}\right)^{\frac{1}{2}}\left(\frac{(2+(\gamma_4-1)}{2+(\gamma_4-1)M_{3a}}\right)^{\frac{2\gamma_4}{\gamma_4-1}}$$

It can be seen from these three equations that Ms and M2 are solely functions of Area Ratio and Pressure Ratio.